Application of the Spectral Element Method to Interior Noise Problems

By

James F. Doyle, Principal Investigator

School of Aeronautics and Astronautics
Purdue University
West Lafayette, Indiana 47907

Final Report:
For the period August 1, 1995 to July 31, 1998

Prepared for:
NASA Langley Research Center
Hampton, VA 23681-0001

Under:
NASA Research Grant NAG 1-1749
Dr. Stephen A. Rizzi, Technical Monitor
Structural Acoustics Branch,
Fluid Mechanics & Acoustics Div.

October 26, 1998

Foreword

This report summarizes the research accomplishments performed under the NASA langley Research Center Grant No. NAG 1-1749, entitled: "Application of the Spectral Element Method to Interior Noise Problems," for the period August 1, 1995 to July 31, 1998. The primary effort of this research project was focused the development of analytical methods for the accurate prediction of structural acoustic noise and response. Of particular interest was the development of curved frame and shell spectral elements for the efficient computational of structural response and of schemes to match this to the surrounding fluid.

Contents

Introduction

This report summarizes research to develop a capability for analysis of interior noise in enclosed structures when acoustically excited by an external random source. Of particular interest was the application to the study of noise and vibration transmission in thin-walled structures as typified by aircraft fuselages.

The basic idea of the research is to reformulate the structure-fluid interaction problem using a matrix methodology based on the spectral element method. In this way, a wave analysis of the problem is retained, yet complex structures can be handled in a convenient manner. The analysis, which is formulated in the frequency domain, is capable of providing detailed information on the response (in either the time or frequency domains) to broad band excitation in any frequency range. The two significant features of the problem, namely; that the loadings on the structure are distributed and that the structures themselves form enclosed cavities (or cabins), are handled well by this formulation.

The spectral element method is a powerful tool for wave propagation problems. It is a matrix method based on wave solutions that exactly satisfy the governing equations and the boundary conditions. That is, the method exactly models the inertia properties and therefore the elements can be large, in fact spanning the region between discontinuities. Consequently, the system size is much smaller compared to a conventional element formulation. Furthermore, the effects of damping, viscoelasticity, and higher order structural models can be easily incorporated in the formulation.

This report focuses on three related topics. The first concerns the development of a curved frame spectral element, the second shows how the spectral element method for wave propagation in folded plate structures is extended to problems involving curved segmented plates. These are of significance because by combining these curved spectral elements with previously presented flat spectral elements, the dynamic response of geometrically complex structures can be determined. The third topic shows how spectral elements, which incorporate the effect of fluid loading on the structure, are developed for analyzing acoustic radiation from dynamically loaded extended plates.

Chapter 1

Deep Curved Beams and Rings

Using the curved beam equivalent of Timoshenko beam theory, the spectral element method is extended to problems involving curved members. By combining these curved beam spectral elements with previously presented straight spectral elements, the dynamic response of geometrically complex structures can be determined. Of particular interest in this paper is the coupling that naturally occurs between the axial and transverse degrees of freedom and how it affects the element formulation. As an example of the utility of this element, the point excitation of an infinite curved beam and a closed ring is demonstrated.

1.1 Introduction

There is considerable intrinsic interest in waves in curved beams because of their use as arches, helical springs and rings, in such structures as aircraft fuselages and ship hulls. Some idea of the range of applications can be found in References [1, 2, 3, 4]. There is also the special case of negligible bending stiffness which corresponds to waves in cables and power lines; an interesting analysis of this is given in Reference [5]. This paper is a continuation of References [6, 7, 8] which developed a matrix methodology for analyzing wave propagation in complex frame structures. Specifically, we extend the spectral element method to include deep curved beam elements.

Two elements are derived: a semi-infinite element, termed a throw-off element, and a finite length element, termed a two-noded element. The throw-off element is important in wave propagation problems since it is used to model remote boundaries which do not reflect waves. Both of these elements exactly model the distribution of mass and rotational inertia and thus can be of any length. While it is possible to model a curved beam as a collection of straight or curved segments, as in conventional element formulations [9, 10], the fact that spectral elements can be very long dictates that we use only one element between any two joints or points of discontinuity.

An interesting aspect of curved beams is the coupling that occurs between the longitudinal and flexural degrees of freedom. The coupling is interesting in the fact that purely axial or transverse excitations will cause both longitudinal and flexural responses in the curved beam. Unlike straight beam modeling where the coupling between the degrees of freedom occurs only at attachment nodes, the curved beam possesses coupling at the differential level. That is, the longitudinal and flexural motion of the curved beam are coupled through the equations of motion, and results in a spectrum relation that is relatively complicated. Therefore a portion of this paper is devoted to discussing the spectrum relation in some detail.

While curved elements can be combined with straight elements to form geometrically complex structures, we will not emphasize that aspect of their use. Rather, we wish to focus specifically on some of the wave propagation aspects. We look at two problems: an infinite curved beam and a closed ring. The infinite beam is used to demonstrate the coupling between the longitudinal and flexural degrees of freedom. The ring illustrates how the point excitation of a simple structure can be viewed as either a wave propagation problem, a vibrations problem, or a rigid body motion problem.

1.2 Spectral Analysis of a Deep Curved Beam

Consider the curved beam segment shown in Figure 1.1. Following Reference [10], the 2-D deformation of the beam can be approximated as

$$\bar{u}(s,y,t) \approx u(s,t) - y\phi(s,t)\,, \qquad \bar{v}(s,y,t) \approx v(s,t)$$

where $u(s,t)$ is the mean mid-plane circumferential displacement, $v(s,t)$ is the radial displacement, and $\phi(s,t)$ is a rotation about the mid-plane. This deformation leads to the non-zero strains

$$\bar{\epsilon}_{ss} = \frac{\partial u}{\partial s} - \frac{v}{R} - y\frac{\partial \phi}{\partial s}\,, \qquad \bar{\gamma}_{sy} = \frac{u}{R} + \frac{\partial v}{\partial s} - \phi$$

Other curved beam theories have slightly different expressions for these strains; the present theory is closest to that of the Timoshenko straight beam [11]. The most significant aspect of this strain-displacement relation is the non-zero centroidal strain (at $y = 0$) even if v is the only deflection. This will give rise to the coupling of the two displacements.

The strain energy for the small segment of curved beam in plane stress is

$$U = \tfrac{1}{2}\int_{\forall}[E\bar{\epsilon}_{ss}^2 + G\bar{\gamma}_{sy}^2]\,d\forall = \tfrac{1}{2}\int_L [EA(\frac{\partial u}{\partial s} - \frac{v}{R})^2 + EI(\frac{\partial \phi}{\partial s})^2 + GAK_1(\frac{u}{R} + \frac{\partial v}{\partial s} - \phi)^2]\,ds$$

where E is the Young's modulus, G is the shear modulus; EA, GAK_1 and EI are the extensional, shear and bending stiffnesses, respectively; $\forall$ is the volume and L the segment length. Note that, as is commonly done, we have associated an adjustable K_1 with the shear stiffness. Typically, this it can be taken close to unity; Reference [11] gives a discussion of the choice of K_1 for the flat Timoshenko beam. The total kinetic energy is

$$T = \tfrac{1}{2}\int_{\forall}\rho[\dot{\bar{u}}^2(s,y,t) + \dot{\bar{v}}^2(s,y,t)]\,d\forall = \tfrac{1}{2}\int_L [\rho A\dot{u}^2 + \rho I K_2\dot{\phi}^2 + \rho A\dot{v}^2]\,ds$$

where ρ is the material density. Here too we introduce an adjustable parameter K_2 to be associated with the rotary inertia. An application of Hamilton's principle [12] using the variations with respect to δu, δv, and $\delta\phi$, leads to the three governing equations of motion (for R=constant)

$$\begin{aligned}
EA\left[\frac{\partial^2 u}{\partial s^2} - \frac{1}{R}\frac{\partial v}{\partial s}\right] - GAK_1\left[\frac{u}{R^2} + \frac{1}{R}\frac{\partial v}{\partial s} - \frac{\phi}{R}\right] &= \rho A\frac{\partial^2 u}{\partial t^2} + \eta A\frac{\partial u}{\partial t} \\
EA\left[\frac{1}{R}\frac{\partial u}{\partial s} - \frac{v}{R^2}\right] + GAK_1\left[\frac{1}{R}\frac{\partial u}{\partial s} + \frac{\partial^2 v}{\partial s^2} - \frac{\partial \phi}{\partial s}\right] &= \rho A\frac{\partial^2 v}{\partial t^2} + \eta A\frac{\partial v}{\partial t} \\
EI\left[\frac{\partial^2 \phi}{\partial s^2}\right] + GAK_1\left[\frac{u}{R} + \frac{\partial v}{\partial s} - \phi\right] &= \rho I K_2\frac{\partial^2 \phi}{\partial t^2} + \eta I K_2\frac{\partial \phi}{\partial t}
\end{aligned} \tag{1.1}$$

where we have added some viscous damping η. The associated natural boundary conditions are given in terms of the resultant forces

$$F \equiv \int_A \sigma_{ss} dA = EA\left[\frac{\partial u}{\partial s} - \frac{v}{R}\right], \qquad V \equiv \int_A \sigma_{sy} dA = GAK_1\left[\frac{u}{R} + \frac{\partial v}{\partial s} - \phi\right] \quad (1.2)$$

and moment

$$M \equiv -\int_A \sigma_{ss} y\, dA = EI\left[\frac{\partial \phi}{\partial s}\right] \quad (1.3)$$

acting on the cross-section, where the integration is over the cross-sectional area A. When R becomes very large, the straight deep beam and elementary rod theories are recovered.

Spectral analysis assumes solutions of the form

$$u(s,t) = \sum \hat{u}(s,\omega)e^{i\omega t}, \qquad v(s,t) = \sum \hat{v}(s,\omega)e^{i\omega t}, \qquad \phi(s,t) = \sum \hat{\phi}(s,\omega)e^{i\omega t} \quad (1.4)$$

where the summations are over frequency. When these are substituted into the governing differential equations, we get a set of ordinary differential equations with constant coefficients. These have solutions of the form

$$\hat{u}(s,\omega) = u_o e^{-iks}, \qquad \hat{v}(s,\omega) = v_o e^{-iks}, \qquad \hat{\phi}(s,\omega) = \phi_o e^{-iks}$$

where $k = k(\omega)$ is the wavenumber. In this representation, the amplitudes u_o, v_o, ϕ_o, and the wavenumber are as yet undetermined. On substitution these lead to the homogeneous system of equations

$$\begin{bmatrix} \alpha_1 - GAK_1/R^2 & (EA+GAK_1)ik/R & GAK_1/R \\ -(EA+GAK_1)ik/R & \alpha_2 - EA/R^2 & ikGAK_1 \\ GAK_1/R & -ikGAK_1 & \alpha_3 - GAK_1 \end{bmatrix} \begin{Bmatrix} u_o \\ v_o \\ \phi_o \end{Bmatrix} = 0 \quad (1.5)$$

with

$$\alpha_1 \equiv -EAk^2 + \rho A\bar{\omega}^2, \qquad \alpha_2 \equiv -GAK_1k^2 + \rho A\bar{\omega}^2, \qquad \alpha_3 \equiv -EIk^2 + \rho IK_2\bar{\omega}^2$$

and $\bar{\omega}^2 \equiv \omega^2 - i\omega\eta/\rho$. For a non-trivial solution, the determinant must be zero and this allows us to determine k. This has six solutions in all, but since only k^2 terms appear, there are three basic modes appearing as $\pm k_m$ pairs.

For each wavenumber k_m, Equation (2.7) gives us the relation among the amplitudes. This is homogeneous and therefore, at best, we can only get amplitude ratios. For example, we can solve for the remaining two terms as a function of u_o. Let us write the solutions at a particular wavenumber k_m as

$$\begin{Bmatrix} u_o \\ v_o \\ \phi_o \end{Bmatrix}_m = \begin{Bmatrix} 1 \\ \Phi_v \\ \Phi_\phi \end{Bmatrix}_m u_o = \{\Phi\}_m u_o$$

where the symbol Φ indicates an amplitude ratio. Although the vector $\{\Phi\}$ shown is normalized with respect to u_o, it is possible for other modal vectors to be normalized differently. This must be done for each mode k_m and hence there are six vectors. We choose to represent these as

$$[\ \Phi\ ] = [[\Phi_A], [\Phi_B]] \equiv \left[\left\{ \begin{array}{c} 1 \\ \Phi_v \\ \Phi_\phi \end{array} \right\}_1 \left\{ \begin{array}{c} \Phi_u \\ 1 \\ \Phi_\phi \end{array} \right\}_2 \left\{ \begin{array}{c} \Phi_u \\ 1 \\ \Phi_\phi \end{array} \right\}_3 \left\{ \begin{array}{c} 1 \\ \Phi_v \\ \Phi_\phi \end{array} \right\}_4 \left\{ \begin{array}{c} \Phi_u \\ 1 \\ \Phi_\phi \end{array} \right\}_5 \left\{ \begin{array}{c} \Phi_u \\ 1 \\ \Phi_\phi \end{array} \right\}_6 \right]$$

where the $[3\times 3]$ partitions $[\Phi_A]$ and $[\Phi_B]$ are evaluated at $+k_m$ and $-k_m$, respectively. The matrices $[\Phi_A]$ and $[\Phi_B]$ are referred to as *modal matrices.* They are fully populated matrices and typically are not symmetric. The normalizations are arranged so that if we set $\Phi_{12} = \Phi_{13} = \Phi_{21} = \Phi_{31} = 0$, the uncoupled straight beam solutions are recovered.

For each mode, the corresponding amplitude u_{om} is undetermined; to make the notation resemble what we have already used, we will label each of the these $\mathbf{A}$, $\mathbf{B}$, $\cdots$. The solution for the displacements can then be expressed as

$$\begin{aligned} \hat{u}(s) &= \mathbf{A}\Phi_{11}e^{-ik_1 s} + \mathbf{B}\Phi_{12}e^{-ik_2 s} + \cdots + \mathbf{E}\Phi_{15}e^{+ik_2 s} + \mathbf{F}\Phi_{16}e^{+ik_3 s} \\ \hat{v}(s) &= \mathbf{A}\Phi_{21}e^{-ik_1 s} + \mathbf{B}\Phi_{22}e^{-ik_2 s} + \cdots + \mathbf{E}\Phi_{25}e^{+ik_2 s} + \mathbf{F}\Phi_{26}e^{+ik_3 s} \\ \hat{\phi}(s) &= \mathbf{A}\Phi_{31}e^{-ik_1 s} + \mathbf{B}\Phi_{32}e^{-ik_2 s} + \cdots + \mathbf{E}\Phi_{35}e^{+ik_2 s} + \mathbf{F}\Phi_{36}e^{+ik_3 s} \end{aligned} \qquad (1.6)$$

where the terms Φ_{ij} are the amplitude ratios. The coefficients $\mathbf{A}, \mathbf{B}, \cdots, \mathbf{F}$ are to be determined from the boundary conditions.

It is apparent that the spectrum relation plays a central role is the solution, and since the characteristic equation is rather complicated, we look at its solution in greater detail next.

1.3 Discussion of the Spectrum Relations

The characteristic equation to determine the wavenumber k is formed by setting the determinant of system (2.7) to zero. To simplify the expressions, first introduce the wavenumbers $k_P^2 \equiv \rho A\bar{\omega}^2/EA$, $k_S^2 \equiv \rho A\bar{\omega}^2/GAK_1$, $k_I^2 \equiv \rho I\bar{\omega}^2/EI$, and $k_B^4 \equiv \rho A\bar{\omega}^2/EI$. On expansion, we find the characteristic equation can be rearranged as

$$k^6 + a_2k^4 + a_1k^2 + a_0 = 0 \tag{1.7}$$

where

$$\begin{aligned} a_2 &= -(k_P^2 + k_S^2 + k_I^2 + 2/R^2) \\ a_1 &= k_P^2k_S^2 + k_P^2k_I^2 + k_S^2k_I^2 - k_B^4 - (k_P^2 + k_S^2 - 2k_I^2)/R^2 + 1/R^4 \\ a_0 &= (-k_P^2 + 1/R^2)(k_S^2k_I^2 - k_B^4 - k_I^2/R^2) \end{aligned}$$

This has six solutions in all, but since only k^2 terms appear, there are three basic modes appearing as $\pm k_i$: one associated with the longitudinal behavior and two associated with the flexural behavior. This can be seen by noting that for very large R the characteristic equation can be factored into

$$(k^2 - k_P^2)[k^4 - (k_S^2 + k_I^2)k^2 - (k_B^4 - k_S^2k_I^2)] = 0$$

where the term in parenthesis is the characteristic equation for the longitudinal motion in a rod [11] and the term in the square brackets is the characteristic equation for the uncoupled flexural response of a Timoshenko beam [6]. In general, of course, the modes are coupled and it is not proper to speak of a longitudinal mode or a flexural mode.

Before we solve for the spectrum relations, it is beneficial to check certain features. First, we see if there is a cut-off frequency; set $k = 0$ in the characteristic equation to get

$$a_0 = (-k_P^2 + 1/R^2)(k_S^2k_I^2 - k_B^4 - k_I^2/R^2) = 0$$

After setting the damping to zero, this yields the two cut-off frequencies,

$$\omega_{c1} = \frac{1}{R}\sqrt{\frac{EA}{\rho A}} = \frac{c_o}{R}, \qquad \omega_{c2} = \sqrt{\frac{GAK_1}{\rho I}\frac{1}{}} + \frac{GAK_1}{\rho AR^2} \approx 2\frac{c_o}{h}$$

where h is the depth of the beam. The presence of a cut-off frequency is typical of elastically coupled systems. It is interesting to note that ω_{c1} depends on the radius of curvature, while ω_{c2} is dominated by the beam depth. It is clear from the expression

for ω_{c2} that for slender beams, this cut-off frequency is very large; this cut-off is associated with the Timoshenko second mode.

Now look at when the frequency is zero, the characteristic equation can be factored as

$$k^2(k^2 - \frac{1}{R^2})(k^2 - \frac{1}{R^2}) = 0$$

Only one root goes through zero, the others are a double root on the real axis.

We must solve a cubic equation in order to get the full behavior of the spectrum relations. The formulas for doing this are more complicated than for the quadratic equation and can be found in Appendix A. Figure 2.2 shows the first three spectrum relations, these correspond to propagating waves, and are characterized by a negative-only imaginary component. To emphasize the coupling, the plot is for an aluminum beam that is $100\,mm\,(4.0\,in)$ deep with a radius of curvature, $R = 100\,mm\,(4.0\,in)$. We clearly see the cut-off frequencies in the first and third modes. Note that k_3 has a negative real component at low frequencies and it might therefore be thought that this violates the radiation condition for waves propagation in the positive direction. In our approach, the wavenumbers always have an imaginary component — even predominantly real-only modes such as k_2 have an imaginary component arising from the damping. Thus the criterion is based on dissipation of energy in the positive direction. A negative real component is expected to lead to a standing wave.

For the later examples, we will use an aluminum beam that is $25.4\,mm\,(1.0\,in)$ deep with a radius of curvature, $R = 254\,mm\,(10.0\,in)$. The spectrum relations for this beam are plotted in Figure 1.3. Only the cut-off frequency in the first mode appears in the frequency range of interest. In the low frequency region $(0-500\,Hz)$, we see some coupling effects due to the thickness of the beam. This coupling diminishes as the radius of curvature increases.

In order to better understand what the spectrum relations are doing, it is worth while to consider a set of approximate spectrum relations. The three roots of the characteristic equation with relatively large R/h ratio can be approximated nicely from the straight beam case as

$$\begin{aligned}
k_1 &= \pm\sqrt{k_P^2 - \frac{1}{R^2}} \\
k_2 &= \pm\sqrt{\frac{1}{2R^2} + \frac{1}{2}(k_I^2 + k_S^2) + \sqrt{k_B^4 + \frac{1}{4}(k_I^2 - k_S^2)^2 + \frac{1}{4R^4}}} \\
k_3 &= \pm\sqrt{\frac{1}{2R^2} + \frac{1}{2}(k_I^2 + k_S^2) - \sqrt{k_B^4 + \frac{1}{4}(k_I^2 - k_S^2)^2 + \frac{1}{4R^4}}}
\end{aligned} \tag{1.8}$$

where k_1 is the longitudinal dominated mode and k_2 and k_3 are the flexural dominated modes. These approximations, also plotted in Figure 1.3, allow us to make a few statements about the behavior of the coupling. In comparison to the uncoupled modes, the major effect is in the longitudinally dominated mode. It can be seen that the behavior is similar to a rod with elastic constraint [11], that is, it is imaginary-only up to the cut-off frequency and then becomes real-only. Thus the low frequency components evanesce indicating a transfer of energy to the other modes. The $1/2R^2$ terms in k_2 and k_3 are acting like a compressive pre-stress on the beam [11]. This has the effect that for the propagating flexural mode the group speed is increased indicating an effective increase in stiffness. However, the coupling generally will not cause drastic changes in the spectrums of the flexural dominated modes. Indeed, if $h \approx R/100$, it is clear from Figure 1.3 that the only difference is in the first mode. Finally, notice how the spectra are almost identical to the uncoupled spectra at the higher frequencies.

1.4 Point Excitation of a Curved Beam

As a prelude to considering curved beams of finite length, we begin by looking at the point excitation of an infinite curved beam; physically this would mean that the beam is in the form of a helix. We will use two types of force histories, one that is relatively broad-banded in frequency and two that are relatively narrow-banded, in order to demonstrate how the coupling of the modes changes with frequency. These are shown, along with their normalized amplitude spectrums, in Figure 1.4.

Our approach to the solution parallels the problems presented in References [6, 8, 11]; what makes this case interesting is that we now have three coupled modes. The solution for the forward propagating terms is written as

$$\begin{aligned}
\hat{u}(s) &= \mathbf{A}\Phi_{11}e^{-ik_1 s} + \mathbf{B}\Phi_{12}e^{-ik_2 s} + \mathbf{C}\Phi_{13}e^{-ik_3 s} \\
\hat{v}(s) &= \mathbf{A}\Phi_{21}e^{-ik_1 s} + \mathbf{B}\Phi_{22}e^{-ik_2 s} + \mathbf{C}\Phi_{23}e^{-ik_3 s} \\
\hat{\phi}(s) &= \mathbf{A}\Phi_{31}e^{-ik_1 s} + \mathbf{B}\Phi_{32}e^{-ik_2 s} + \mathbf{C}\Phi_{33}e^{-ik_3 s}
\end{aligned} \tag{1.9}$$

From the free body diagram of the excitation region of the infinite beam it can be shown that at the loading site $s = 0$,

$$u(0,t) = 0, \qquad \phi(0,t) = 0, \qquad V(0,t) = -\tfrac{1}{2}P(t)$$

where we are considering a transverse impact. The first two of these allow the solution to be written as

$$\begin{aligned}
\hat{u}(s) &= \mathbf{A}[\Phi_{11}e^{-ik_1 s} + \alpha\Phi_{12}e^{-ik_2 s} + \beta\Phi_{13}e^{-ik_3 s}] \\
\hat{v}(s) &= \mathbf{A}[\Phi_{21}e^{-ik_1 s} + \alpha\Phi_{22}e^{-ik_2 s} + \beta\Phi_{23}e^{-ik_3 s}] \\
\hat{\phi}(s) &= \mathbf{A}[\Phi_{31}e^{-ik_1 s} + \alpha\Phi_{32}e^{-ik_2 s} + \beta\Phi_{33}e^{-ik_3 s}]
\end{aligned}$$

where the coefficients α and β are given by

$$\alpha = -\frac{\Phi_{11}\Phi_{33} - \Phi_{31}\Phi_{13}}{\Phi_{12}\Phi_{33} - \Phi_{32}\Phi_{13}}, \qquad \beta = -\frac{\Phi_{11}\Phi_{32} - \Phi_{31}\Phi_{12}}{\Phi_{13}\Phi_{32} - \Phi_{33}\Phi_{12}}$$

We determine $\mathbf{A}$ from the shear relation

$$-\tfrac{1}{2}P = V = GAK_1\left[\frac{u}{R} + \frac{\partial v}{\partial s} - \phi\right]$$

After differentiation, this leads to

$$\mathbf{A} = \frac{-\hat{P}}{2GAK_1[q_1 + \alpha q_2 + \beta q_3]}, \qquad q_m = \frac{1}{R}\Phi_{1m} - ik_1\Phi_{2m} - \Phi_{3m}$$

The solution is arranged so that if we set $R = \infty$ then $\Phi_{12} = \Phi_{13} = \Phi_{21} = \Phi_{31} = 0$, and the uncoupled straight beam solution is recovered. Care must be taken, however, in order to approach the proper limit since both α and *beta* approach infinity. It turn out that $\alpha/\beta = 1$ in the limit and we get, for example,

$$\hat{\phi}(s) = \frac{-\hat{P}}{2EI(k_2^2 - k_3^3)}[e^{-ik_2 s} - e^{-ik_3 s}]$$

Note that the spectrum relations also change.

The velocity reconstructions for the broad band input are shown in Figure 3.2. There are two points of interest. First, note how the initial zero axial velocity eventually becomes significant. Second, note the oscillatory behavior of the transverse velocity. Although the force excitation lasts only about $200\,\mu s$, the beam near $s = 0$ continues to oscillate in an almost resonant like fashion. Actually, a standing wave has been established. The figure also shows the separate contributions from each mode for the response $v(s = 3R, t)$. It is clear that the first mode is contributing the ringing behavior.

This is more evident when we look at these velocity responses in the frequency domain. It is clear in Figure 2.8 that there is a peak in the v-velocity response which corresponds with the cut-off frequency. Furthermore, this peak is coming entirely from the first mode. The broadband excitation has identified the cut-off frequency in the first mode.

A final point of interest for this example looks further at the effect of the cut-off frequency in the longitudinal mode. Below this frequency there is only one propagating mode in the beam, while above the frequency two propagating modes exist. To illustrate this point, we excite the curved beam with the narrow banded force histories shown in Figure 1.4. The pulses are chosen so that they just bracket the cut-off frequency. Figure 1.7 clearly shows the presence of the second propagating mode above the cut-off frequency. Note that the two propagating modes are present in both the transverse and longitudinal responses but the amplitude ratios are different. This plot is emphasizing the nature of the solution of Equation (2.8) as a collection of mode responses.

1.5 Spectral Element Formulation

As seen from the point excitation example of the last section, the formulation, although relatively straight forward, requires a significant amount of manipulation. A similar approach for connected curved beams or even for a finite curved beam would be very cumbersome, hence we now develop a matrix formulation to facilitate these manipulations.

Consider a segment of curved beam of length L. We begin by expressing the displacements as

$$\begin{aligned}
\hat{u}(s) &= \mathbf{A}\Phi_{11}e^{-ik_1 s} + \mathbf{B}\Phi_{12}e^{-ik_2 s} + \cdots + \mathbf{E}\Phi_{15}e^{-ik_2(L-s)} + \mathbf{F}\Phi_{16}e^{-ik_3(L-s)} \\
\hat{v}(s) &= \mathbf{A}\Phi_{21}e^{-ik_1 s} + \mathbf{B}\Phi_{22}e^{-ik_2 s} + \cdots + \mathbf{E}\Phi_{25}e^{-ik_2(L-s)} + \mathbf{F}\Phi_{26}e^{-ik_3(L-s)} \\
\hat{\phi}(s) &= \mathbf{A}\Phi_{31}e^{-ik_1 s} + \mathbf{B}\Phi_{32}e^{-ik_2 s} + \cdots + \mathbf{E}\Phi_{35}e^{-ik_2(L-s)} + \mathbf{F}\Phi_{36}e^{-ik_3(L-s)} \quad (1.10)
\end{aligned}$$

The length is introduced to include reflections coming from a boundary located at $s = L$. This displacement solution can now be re-written as

$$\begin{aligned}
\{u(s),\, v(s),\, \phi(s)\}^T &= \{\mathcal{U}\}(s) \\
&= \{\Phi\}_1 \mathbf{A}e^{-ik_1 s} + \cdots + \{\Phi\}_6 \mathbf{F}e^{-ik_3(L-s)}
\end{aligned}$$

We will re-write this in an even more compact matrix form; so as to make the matrix notation a little more accessible, we will take the developments of the rod as the archetype and use its notation (except changed to matrices). The 1-D solution for a rod [11] is represented as

$$\hat{u}(x) = [e^{-ik_1 x}]\mathbf{A} + [e^{-ik_1(L-x)}]\mathbf{B}$$

where **A** and **B** are associated with the forward moving and backward moving waves, respectively. The displacement for the curved beam is written as

$$\{\mathcal{U}\}(s) = [\Phi_A]\lceil e(s)\rfloor\{\mathbf{A}\} + [\Phi_B]\lceil e(L-s)\rfloor\{\mathbf{B}\}$$

were $[\Phi_A]$ or $[\Phi_B]$ are the $[3 \times 3]$ partitions of $[\ \Phi\ ]$ and

$$\lceil e(s)\rfloor \equiv \begin{bmatrix} e^{-ik_1 s} & 0 & 0 \\ 0 & e^{-ik_2 s} & 0 \\ 0 & 0 & e^{-ik_3 s} \end{bmatrix}, \qquad \{\mathbf{A}\} \equiv \begin{Bmatrix} \mathbf{A} \\ \mathbf{B} \\ \mathbf{C} \end{Bmatrix}, \qquad \{\mathbf{B}\} \equiv \begin{Bmatrix} \mathbf{D} \\ \mathbf{E} \\ \mathbf{F} \end{Bmatrix}$$

It is the presence of the amplitude ratios that is the most significant difference.

We wish to replace the vectors $\{\mathbf{A}\}$ and $\{\mathbf{B}\}$ in terms of the nodal displacements at $s = 0$ and $s = L$. That is, we introduce

$$\hat{u}(0) = \hat{u}_1\,, \quad \hat{v}(0) = \hat{v}_1\,, \quad \hat{\phi}(0) = \hat{\phi}_1\,; \qquad \hat{u}(L) = \hat{u}_2\,, \quad \hat{v}(L) = \hat{v}_2\,, \quad \hat{\phi}(L) = \hat{\phi}_2$$

We write this in matrix notation as

$$\begin{aligned}\{\hat{u}_1,\, \hat{v}_1,\, \hat{\phi}_1\}^T = \{u\}_1 = \{u\}(s=0) &= [\Phi_A]\lceil e(0)\rfloor\{\mathbf{A}\} - [\Phi_B]\lceil e(L)\rfloor\{\mathbf{B}\} \\ \{\hat{u}_2,\, \hat{v}_2,\, \hat{\phi}_2\}^T = \{u\}_2 = \{u\}(s=L) &= [\Phi_A]\lceil e(L)\rfloor\{\mathbf{A}\} - [\Phi_B]\lceil e(0)\rfloor\{\mathbf{B}\}\end{aligned}$$

Let us write all six equations as

$$\left\{ \begin{matrix} \{u\}_1 \\ \{u\}_2 \end{matrix} \right\} = [\, Q \,] \left\{ \begin{matrix} \{\mathbf{A}\} \\ \{\mathbf{B}\} \end{matrix} \right\}$$

Solving for the coefficients gives

$$\left\{ \begin{matrix} \{\mathbf{A}\} \\ \{\mathbf{B}\} \end{matrix} \right\} = [Q^{-1}] \left\{ \begin{matrix} \{u\}_1 \\ \{u\}_2 \end{matrix} \right\} = [\, G \,] \left\{ \begin{matrix} \{u\}_1 \\ \{u\}_2 \end{matrix} \right\} = \left[\begin{matrix} [G_{11}] & [G_{12}] \\ [G_{21}] & [G_{22}] \end{matrix} \right] \left\{ \begin{matrix} \{u\}_1 \\ \{u\}_2 \end{matrix} \right\}$$

where each partition of $[\, G \,]$ is of size $[3 \times 3]$. We are now in a position to write the displacements in terms of the shape functions. They are

$$\{\mathcal{U}\}(s) = [g(s)]_1\{u\}_1 + [g(s)]_2\{u\}_2 \tag{1.11}$$

where the $[3 \times 3]$ matrix of shape functions are defined as

$$\begin{aligned}[g(s)]_1 &= [\Phi_A]\lceil e(s)\rfloor[G_{11}] + [\Phi_B]\lceil e(L-s)\rfloor[G_{21}] \\ [g(s)]_2 &= [\Phi_A]\lceil e(s)\rfloor[G_{12}] + [\Phi_B]\lceil e(L-s)\rfloor[G_{22}]\end{aligned} \tag{1.12}$$

There are a total of $3 \times 3 \times 2 = 18$ shape functions in all. While not obvious from the above, it turns out that, even in this general case, the collection of shape functions associated with the degrees of freedom at the second node are the mirror image of the first set.

Figure 3.6 shows the $g_{22}(s)$ shape function of a 270° beam segment at a number of frequencies. This shape function is associated with the $\hat{v}_1$ degree of freedom and thus can be plotted as a radial displacement off the original shape. It is similar to conventional shape functions except that it is frequency dependent, typically complex, and can represent the behavior of very large beam segments. The other shape functions behave in a similar manner. It is clear from this figure and from the above developments, that once the nodal degrees of freedom are determined that the shape functions can be used to compute the responses at any intermediate locations. This is a crucial attribute since the beam segments or elements can be very long.

The next step in the element development is to derive a stiffness relation for the beam segment. The process is simply that of expressing the resultant forces and moments from Equations (2.5) and (1.3) in terms of the displacement solutions given

in Equation (2.12). We can write resultants associated with the boundary conditions in terms of the displacements in matrix form as

$$\{\mathcal{F}\}(s) = \{F,\, V,\, M\}^T(s) = [\ \partial\ ]\{\mathcal{U}\}(s)$$

where $[\ \partial\ ]$ is the matrix collection of differential operators of size $[3 \times 3]$. After substituting for $\{\mathcal{U}\}(s)$ in terms of the shape functions get

$$\begin{aligned} \{\mathcal{F}\}(s) &= [\ \partial\ ][g(s)]_1\{u\}_1 + [\ \partial\ ][g(s)]_2\{u\}_2 \\ &\equiv [\partial g(s)]_1\{u\}_1 + [\partial g(s)]_2\{u\}_2 \end{aligned} \tag{1.13}$$

Relating the member resultants at $s = 0$ and $s = L$ to the nodal loads at the same locations leads to the stiffness relation

$$\begin{Bmatrix} \{F\}_1 \\ \{F\}_2 \end{Bmatrix} = \begin{bmatrix} [-\partial g(0)]_1 & [-\partial g(0)]_2 \\ [+\partial g(L)]_1 & [+\partial g(L)]_2 \end{bmatrix} \begin{Bmatrix} \{u\}_1 \\ \{u\}_2 \end{Bmatrix} \tag{1.14}$$

or simply

$$\{\hat{F}\} = [\hat{k}(\omega)]\{\hat{u}\}\,, \qquad \{\hat{F}\} = \{\hat{F}_1,\, \hat{V}_1,\, \hat{M}_1;\, \hat{F}_2,\, \hat{V}_2,\, \hat{M}_2\}^T\,, \quad \{\hat{u}\} \equiv \{\hat{u}_1,\, \hat{v}_1,\, \hat{\phi}_1;\, \hat{u}_2,\, \hat{v}_2,\, \hat{\phi}_2\}^T$$

where $[\ \hat{k}\ ]$ is the $[6 \times 6]$ dynamic element stiffness matrix. This stiffness matrix is frequency dependent, complex, and symmetric.

For illustrative purposes, Figure 2.4 shows the normalized $\hat{k}_{11}$, $\hat{k}_{22}$, and $\hat{k}_{33}$ diagonal terms for the same beam used to illustrate the shape functions. As is typical with spectral elements, they exhibit a very large dynamic range. The normalizations are with respect to the stiffnesses for straight thin beams [12]. That is, they are presented as

$$\hat{k}_{11}/(EA/L)\,, \qquad \hat{k}_{22}/(12EI/L^3)\,, \qquad \hat{k}_{33}/(12EI/L)$$

Note that the $\hat{k}_{11}$ stiffness is substantially less than the elementary rod values, and it is only after the cut-off frequency ($\approx 3\,kHz$) does it become greater than unity. This can be understood by considering the static (low-frequency) axial loading of the beam fixed at one end — because of the curvature, the axial load creates a moment and consequently, the beam has a great deal more flexibility than the corresponding straight case.

The stiffness relation for the throw-off or semi-infinite element is simply

$$\{F\}_1 = [-\partial g(0)]_1\{u\}_1 = [\hat{k}(\omega)]\{u\}_1\,, \qquad [g(s)]_1 = [\Phi_A]\lceil e(s)\rfloor[G_{11}] \tag{1.15}$$

The stiffness matrix in this case is a $[3 \times 3]$ frequency dependent, complex and symmetric matrix. This can be used to recover the results presented for the impact of an infinite or semi-infinite curved beam

1.6 Point Excitation of a Closed Ring

The advantage of the curved element is that it can be combined with other elements, either flat or curved to form significantly more complex structures. References [6, 13] discuss the programming structure required for multiply connected spectral elements. However, we will not emphasize this aspect of their use, rather, we will perform the example of the point excitation of a closed ring. The example demonstrates the basic method of joining elements in addition to demonstrating the utility of the spectral method.

We form the closed ring by combining two curved elements of the same material properties each of which is a half-circle. Because of symmetry, we could model the ring with a single half-circle element or as a single whole-circle element. In the latter case half of the applied load must be placed at each node and the extra conditions of $u_1 = 0$, $\phi_1 = 0$; $u_2 = 0$, $\phi_2 = 0$ be imposed. The two element model was chosen so as to verify the assemblage process.

The elements can be joined at the common nodes by merely summing together the appropriate dynamic stiffness matrix components to form a global stiffness matrix $[\,\hat{K}\,]$. We must therefore first rotate each element stiffness to this global system. The transformation requires the use of a simple $[6 \times 6]$ rotation matrix $[\,T\,]$ that is of the form

$$[\,T\,] = \begin{bmatrix} [R(\alpha)] & 0 \\ 0 & [R(\alpha + 2\beta)] \end{bmatrix}$$

where $R(\theta)$ is the $[3 \times 3]$ rotation matrix [12]. This takes into account that the ends of the curved element are oriented differently to each other. In the plane case, if the nodal coordinates are (x_1, y_1) and (x_2, y_2), then with $2p = \sqrt{(x_2 - x_1)^2 + (y_2 - y_1)^2}$ and $q = \sqrt{R^2 - p^2}$, the angles are given by

$$\alpha = \tan^{-1}\left(\frac{(x_2 - x_1)p - (y_2 - y_1)q}{(x_2 - x_1)q + (y_2 - y_1)p}\right), \qquad \beta = \tan^{-1}\left(\frac{p}{q}\right)$$

Since only two elements are present, we will assign the coordinate system of one to be the global coordinate system and rotate the other.

The matrix $[\,T\,]$ transforms the vectors of nodal displacements and nodal forces to the global system as follows

$$\{\hat{F}\} = [\,T\,]\{\hat{\bar{F}}\}, \qquad \{\hat{u}\} = [\,T\,]\{\hat{\bar{u}}\}$$

where the barred quantities represent the local coordinate system. As a consequence, the element stiffness matrix in global coordinates can be written as

$$[\,\hat{k}\,] = [\,T\,]^T[\,\hat{\bar{k}}\,][\,T\,]$$

The global stiffness matrix is then simply formed by adding the two global element stiffness matrices together.

With the elements connected, we can now determine the responses of the closed ring due to a point excitation. The velocity reconstructions for three points, $\theta = 0^o$, 90^o, 180^o, along the ring are shown in Figure 2.5. For comparison purposes, the same ring was modeled using 64 straight Timoshenko spectral elements. The two sets of results are indistinguishable.

Unlike the previous example of an infinite curved beam, there are multiple reflections occurring. The waves are traveling around the ring and interacting with each other. From Figure 2.6, we can see that many resonance frequencies are being established. These would be the frequencies of interest if a vibration experiment were being performed. It is interesting to note that the v response at 90^o is missing many of the intermediate resonances, but these are present in the u response. Furthermore, we see the effect of the first mode cut-off frequency in the v responses but not in u. This is consistent with Figure 2.8 for the infinite beam.

As a final illustration of the results, we integrate the velocity responses for the ring to determine how it is deforming over time. Figure 1.12 illustrates the exaggerated deformation (multiplication by 300) of the ring due to the point excitation. It is interesting to note the rigid body motion that is occurring although it was not specifically addressed in the solution. On the time scale shown, the problem reduces simply to a transfer of momentum. The force transfers an impulse of about $0.31\,Ns$ to the ring of mass $2.80\,kg$, thus the force should cause the ring to move at about $113\,mm/s$. From the figure, we can approximate the ring velocity as $103\,mm/s$, the difference being due to the damping present in the modeling.

The flexibility of the spectral element approach has allowed us to view the problem of the impact of a ring as one of wave propagation, or vibration, or rigid body dynamics. This comes about because of the convenience in alternating between the time and frequency domains.

1.7 Discussion

A deep curved beam element was developed that extends the variety of problems the spectral element method can handle. One of the challenges that arose during the development was the problem of determining the spectrum relations. Even though cubic solvers are well known, it is not always certain which branch should be chosen after a branch point occurs. In the quadratic case, which occurs for straight beams, the ambiguity is removed by adding damping. This becomes essential in the cubic case so that the phase of each $k_m(\omega)$ can be tracked correctly. The effect of the damping is to separate each of the modes. With this separation, we can also reliably identify the associated amplitude ratios.

The element developed possesses all of the features of the spectral element method which make the method desirable for solving dynamic problems. Primary among these are that the element can be very long and that the frequency domain formulation allows the system response functions to be determined automatically. This latter attribute, along with the fast Fourier transform, enables a duality between the time domain and frequency domain to be presented conveniently. Information not readily seen in one is often detectable in the other. The example problems demonstrate these features.

Appendix A: Computing the Spectrum Relations

The formulas used to solve the characteristic equation are based on References[14, 15]. By replacing k^2 with z, the characteristic equation can be re-written as

$$z^3 + a_2 z^2 + a_1 z + a_0 = 0$$

where the coefficients are insured of being complex by adding damping to the system. Now compute the terms

$$q = (a_2^2 - 3a_1)/9\,, \qquad r = (2a_2^3 - 9a_2 a_1 + 27a_0)/54$$

and

$$s_1 = -[r + \sqrt{r^2 - q^3}]^{1/3}\,, \qquad s_2 = \frac{-q}{[r + \sqrt{r^2 - q^3}]^{1/3}}$$

The three roots are then given by

$$\begin{aligned} z_1 &= (s_1 + s_2) - \tfrac{1}{3}a_2 \\ z_2 &= -\tfrac{1}{2}(s_1 + s_2) - \tfrac{1}{3}a_2 + i\tfrac{1}{2}(s_1 - s_2)\sqrt{3} \\ z_3 &= -\tfrac{1}{2}(s_1 + s_2) - \tfrac{1}{3}a_2 - i\tfrac{1}{2}(s_1 - s_2)\sqrt{3} \end{aligned}$$

The six spectrum relations are given as $\pm\sqrt{z}$.

A difficulty arises in choosing the appropriate square or cube root since we wish to compute single z_j at a time. The issue is that while the n^{th} root of a complex number z is given by

$$z = a + ib = Ae^{i\phi}\,, \qquad z^{1/n} = A^{1/n} e^{i\phi/n}$$

the phase $\phi = \tan^{-1}(b/a)$ has an ambiguity of $N\pi$. We remove this ambiguity by keeping track of the total phase. That is, starting with some value and with reference to the unit circle in the complex plane, as the wavenumber goes from the 4^{th} to the 1^{st} quadrant the total phase is increased by 2π. Conversely, if the wavenumber goes from the 1^{st} to the 4^{th} quadrant the total phase is decreased by 2π. The n^{th} root is then given by

$$z^{1/n} = A^{1/n} e^{i(\phi + N\pi)/n}$$

This scheme works quite robustly when the frequency increment is not too large.

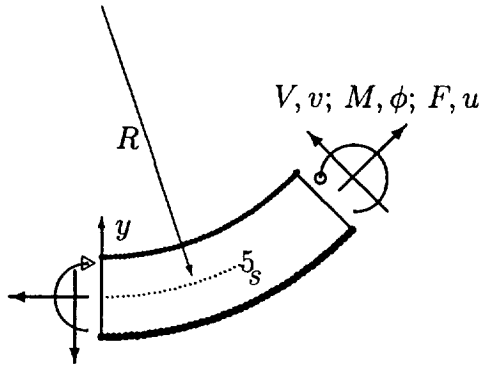

Figure 1.1: Coordinate system and resultant loads for a deep curved beam.

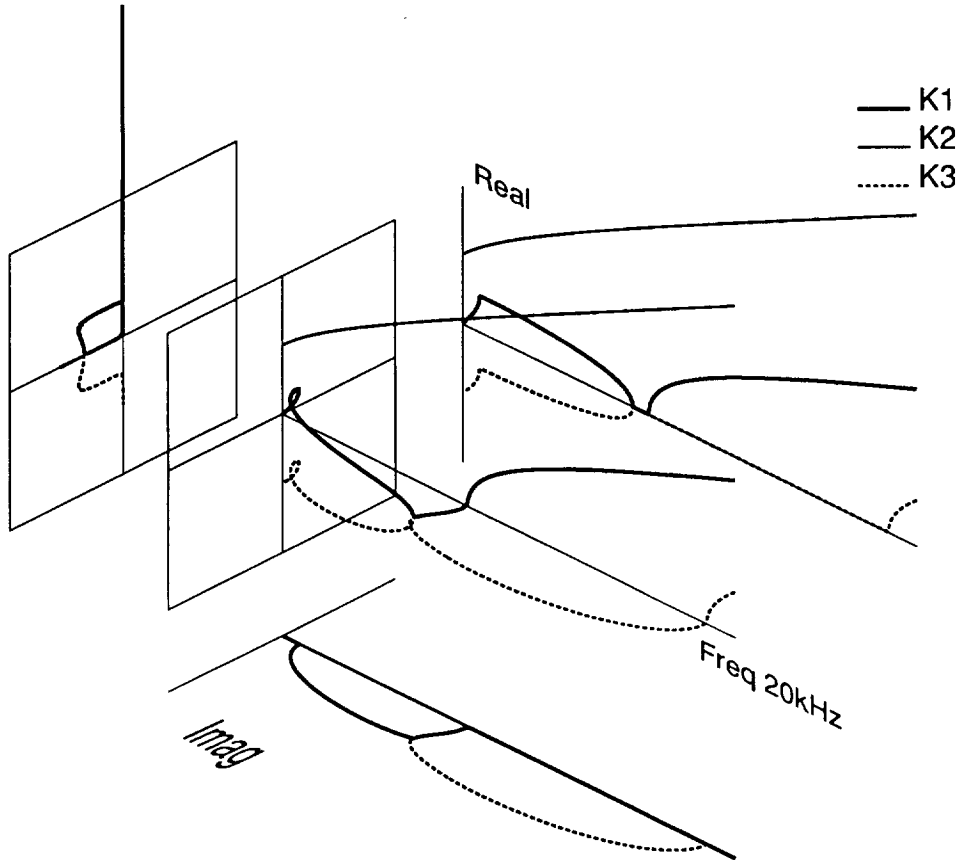

Figure 1.2: Spectrum relations kh for a curved beam with $R = 100\,mm$ and $h = 100\,mm$.

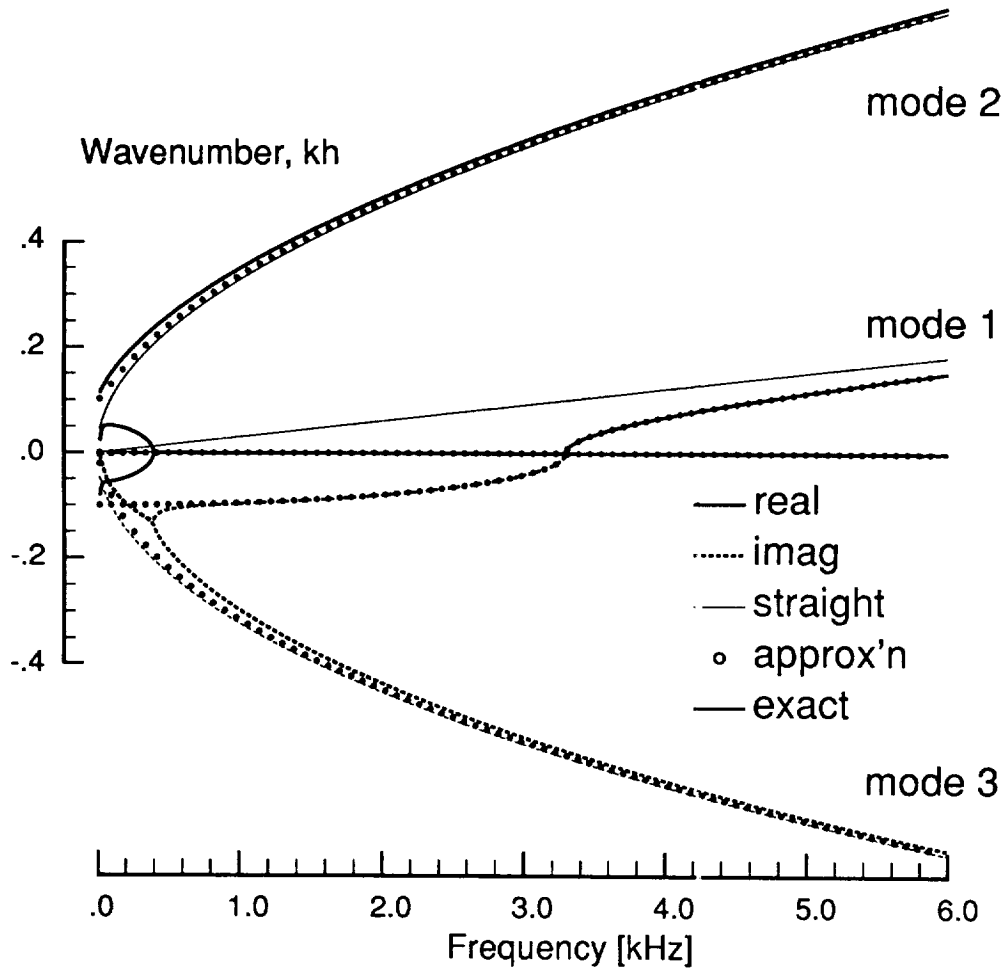

Figure 1.3: Spectrum relations kh for a curved beam with $R = 254\,mm$ and $h = 25.4\,mm$.

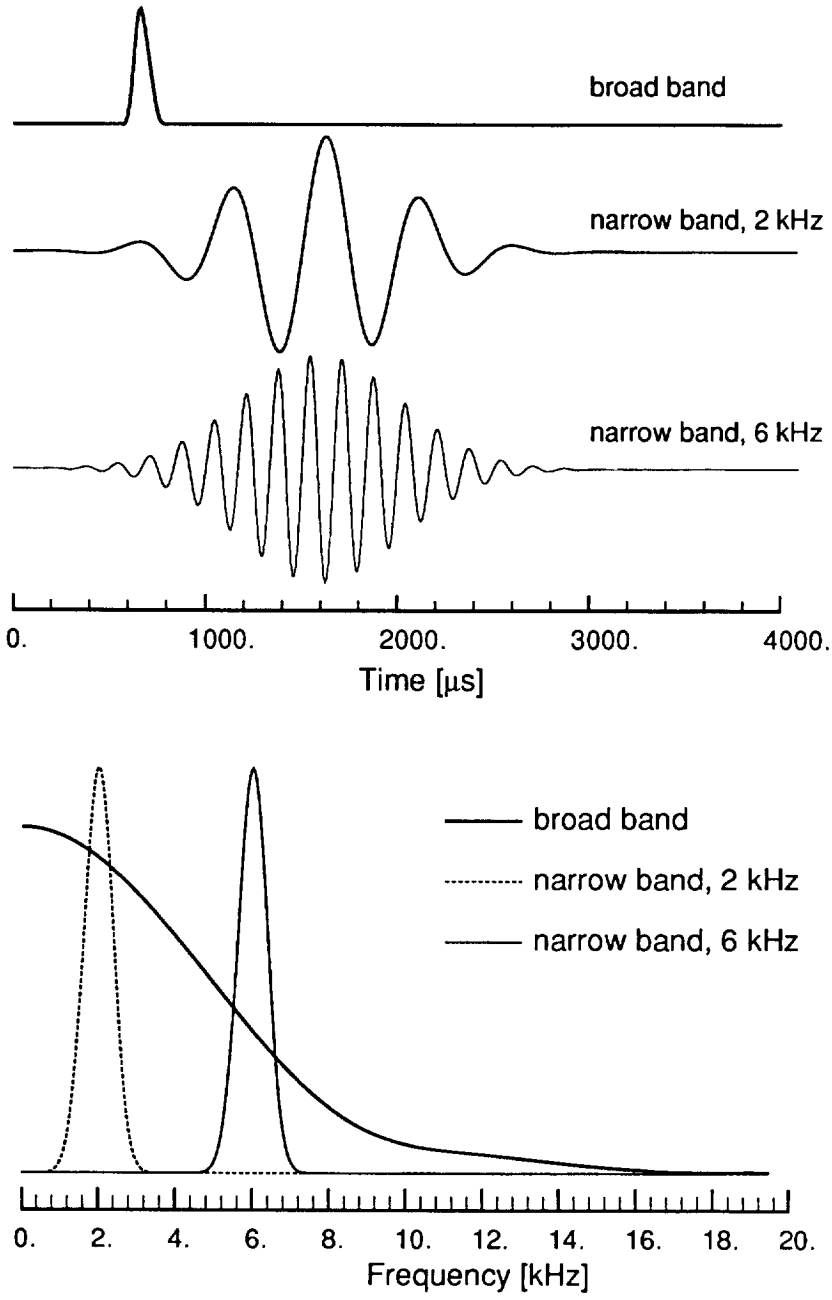

Figure 1.4: Force histories and corresponding amplitude spectrums.

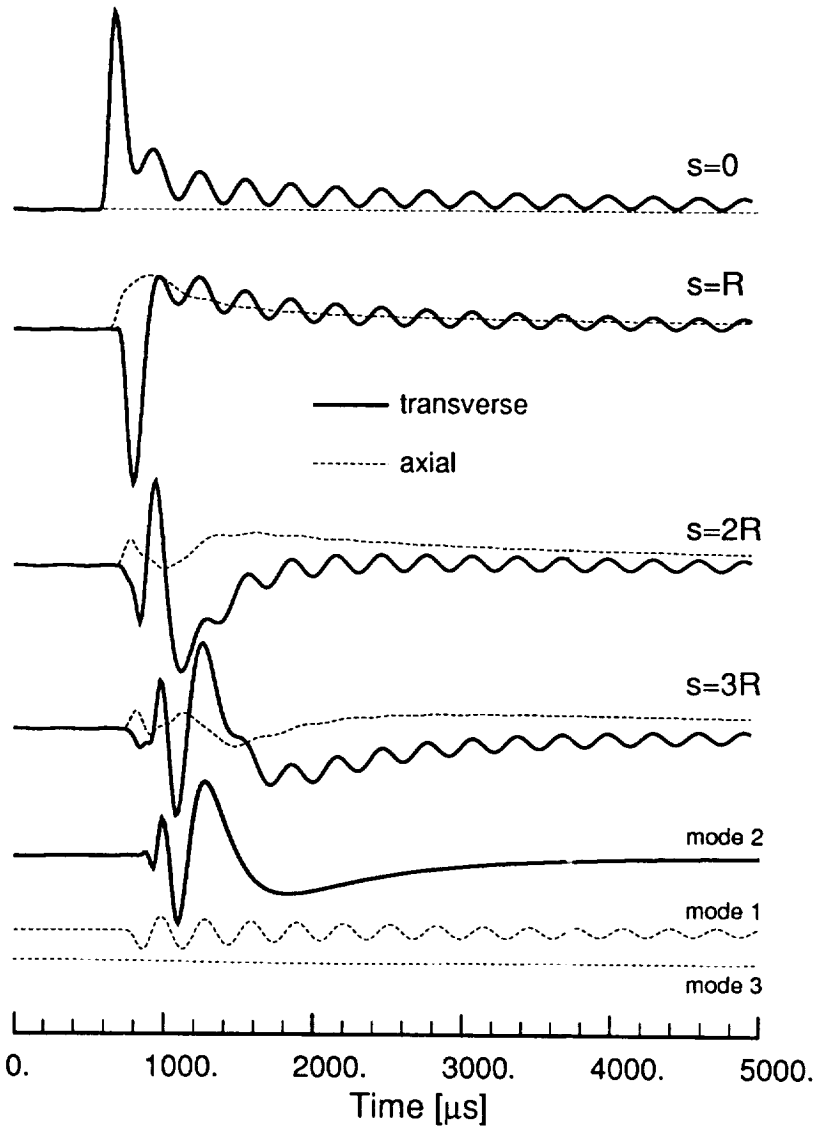

Figure 1.5: Velocity reconstructions for the point excitation of an infinite curved beam.

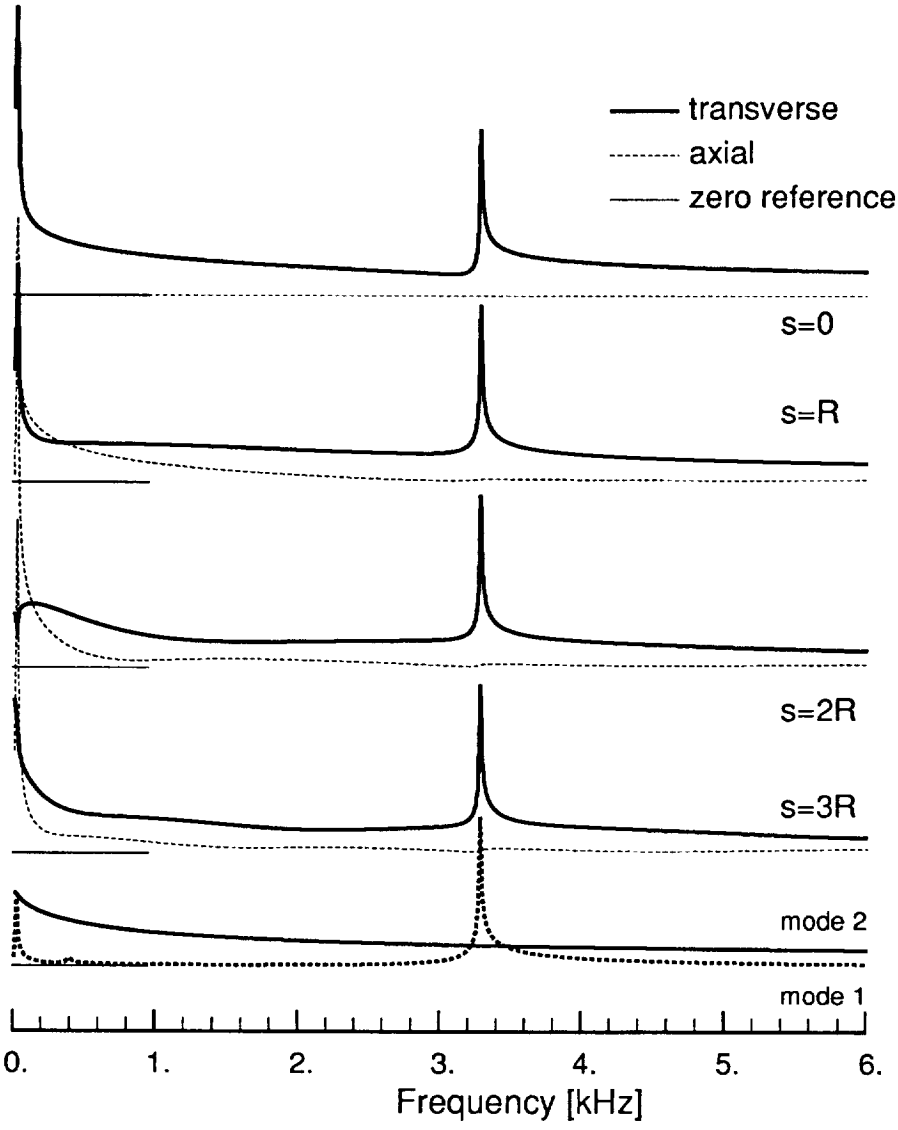

Figure 1.6: Frequency domain response for the point excitation of an infinite curved beam.

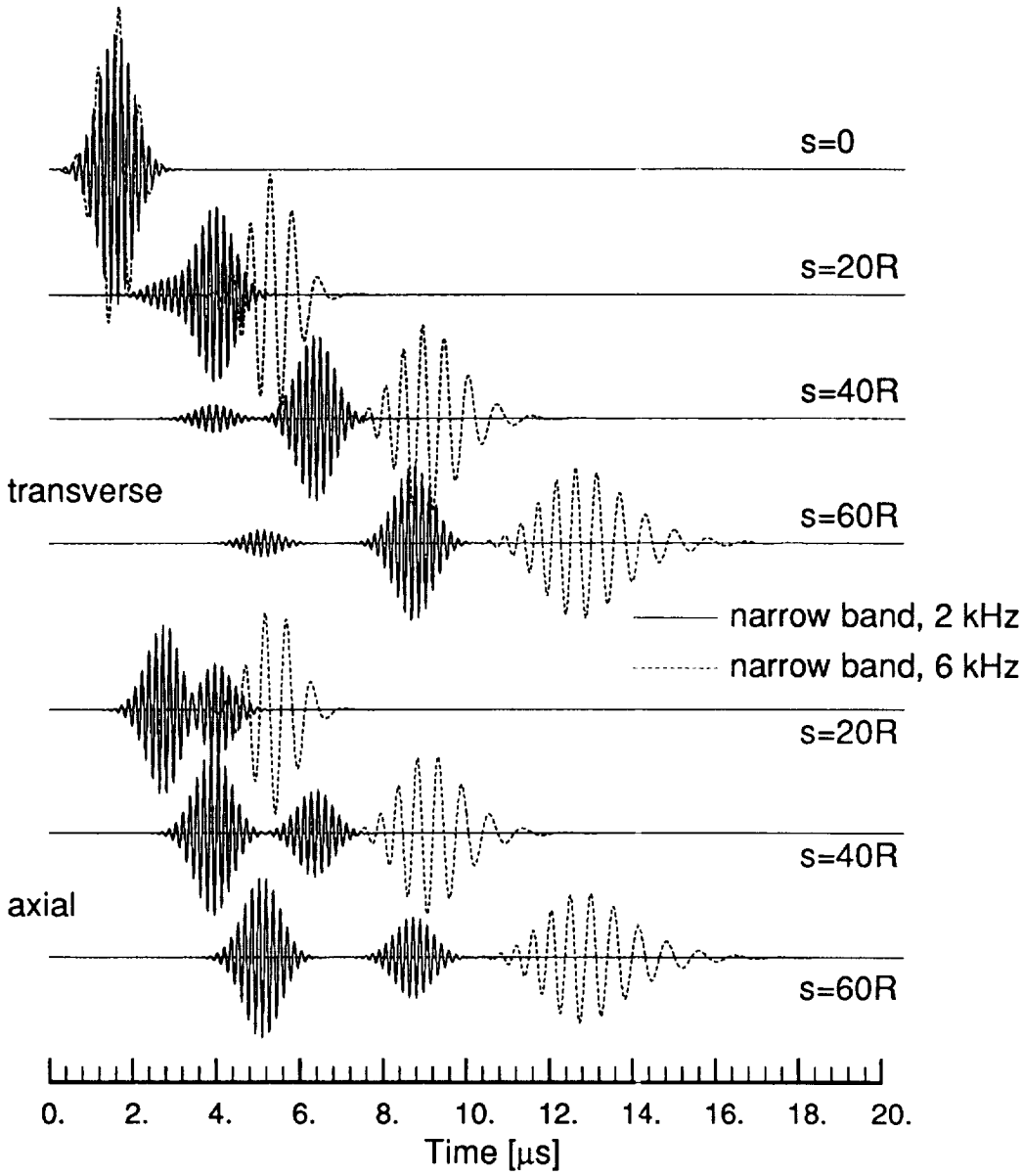

Figure 1.7: Velocity responses due to narrow banded point excitations.

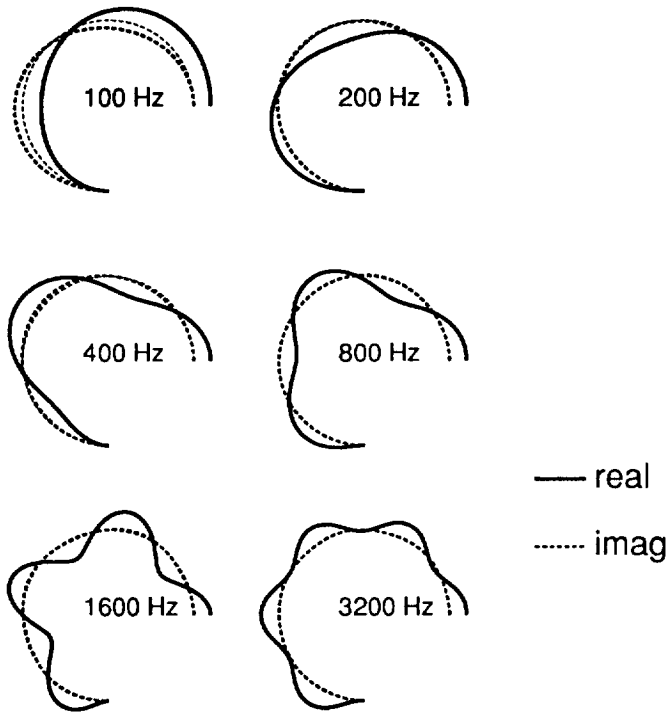

Figure 1.8: Shape functions for a 270^o curved beam element.

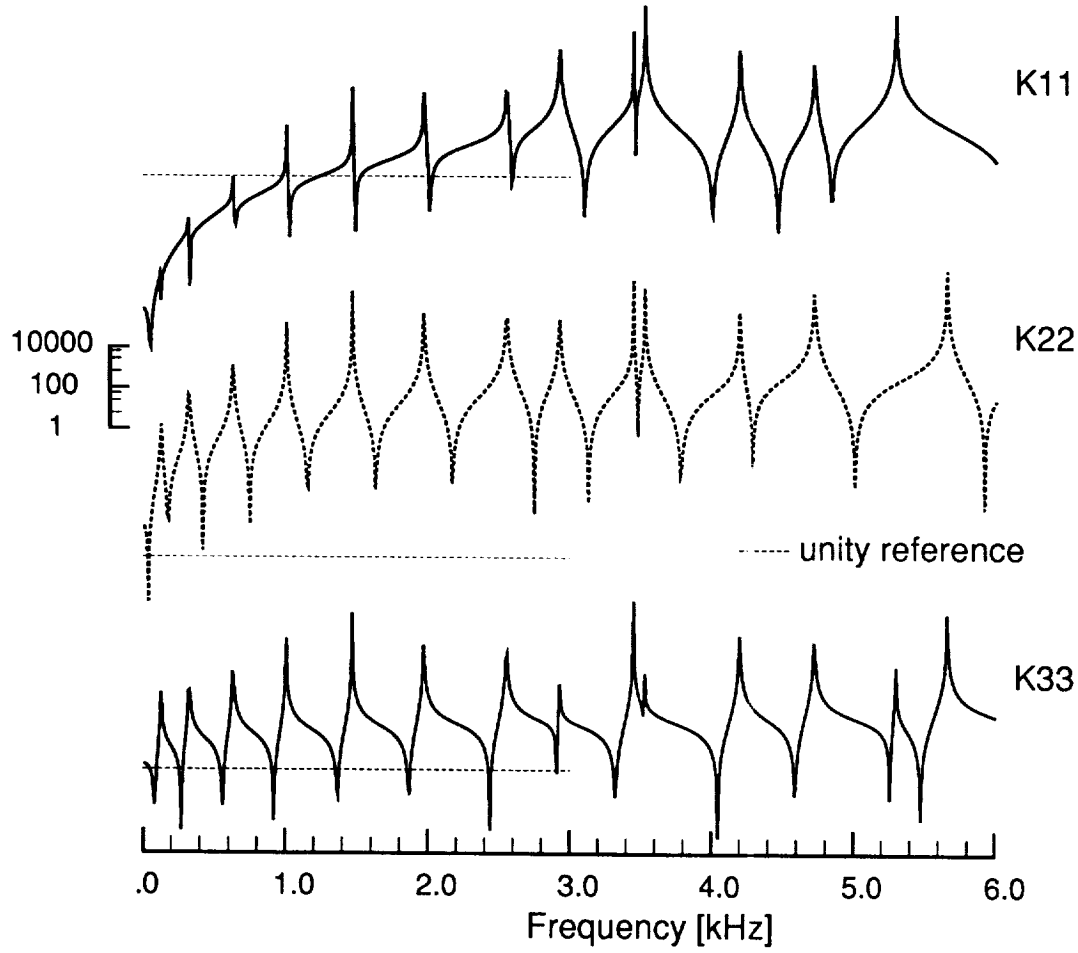

Figure 1.9: Normalized stiffnesses $\hat{k}_{11}$, $\hat{k}_{22}$, and $\hat{k}_{33}$ for a 270^o curved beam element.

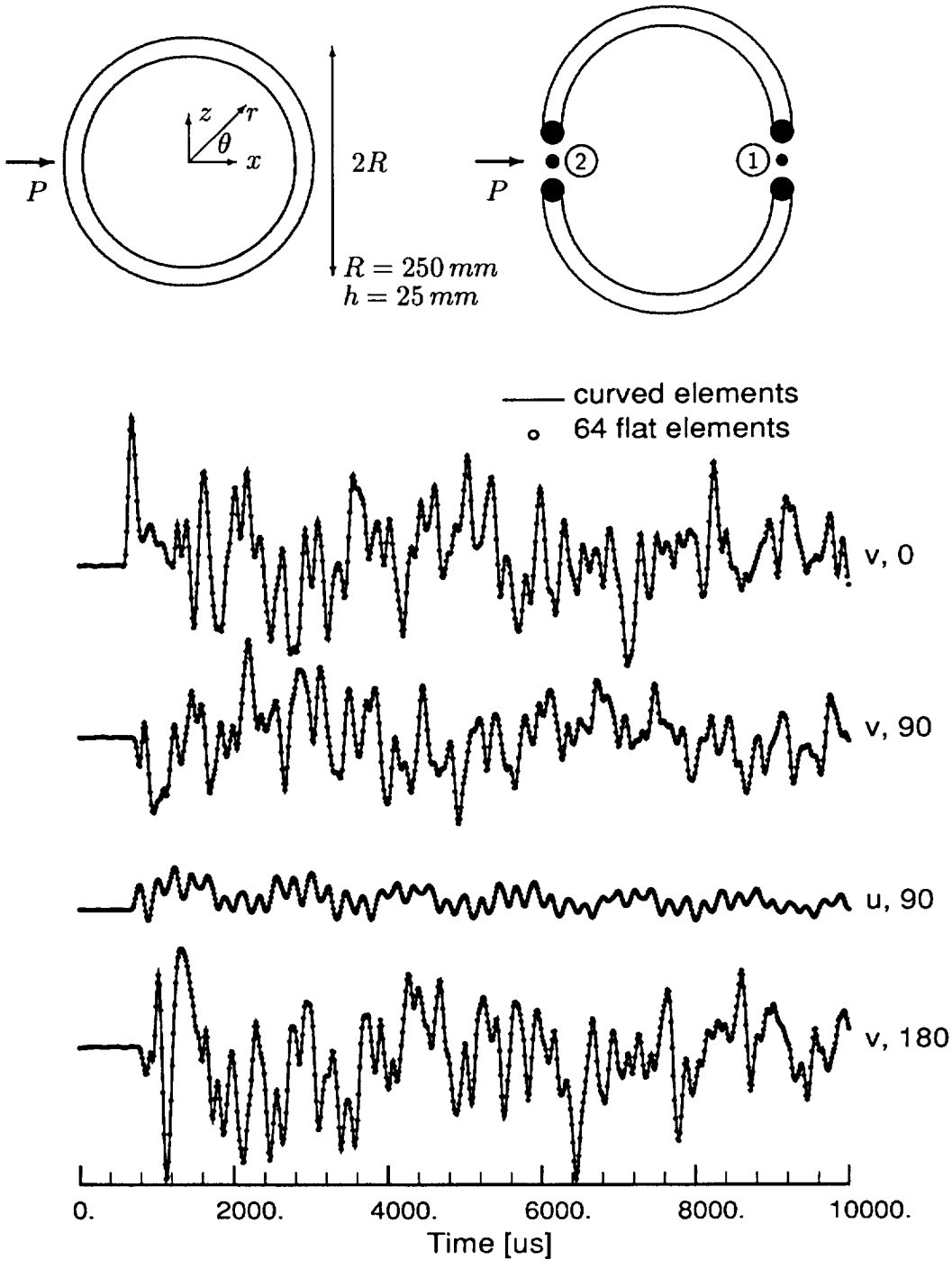

Figure 1.10: Velocity reconstructions for the point excitation of a closed ring.

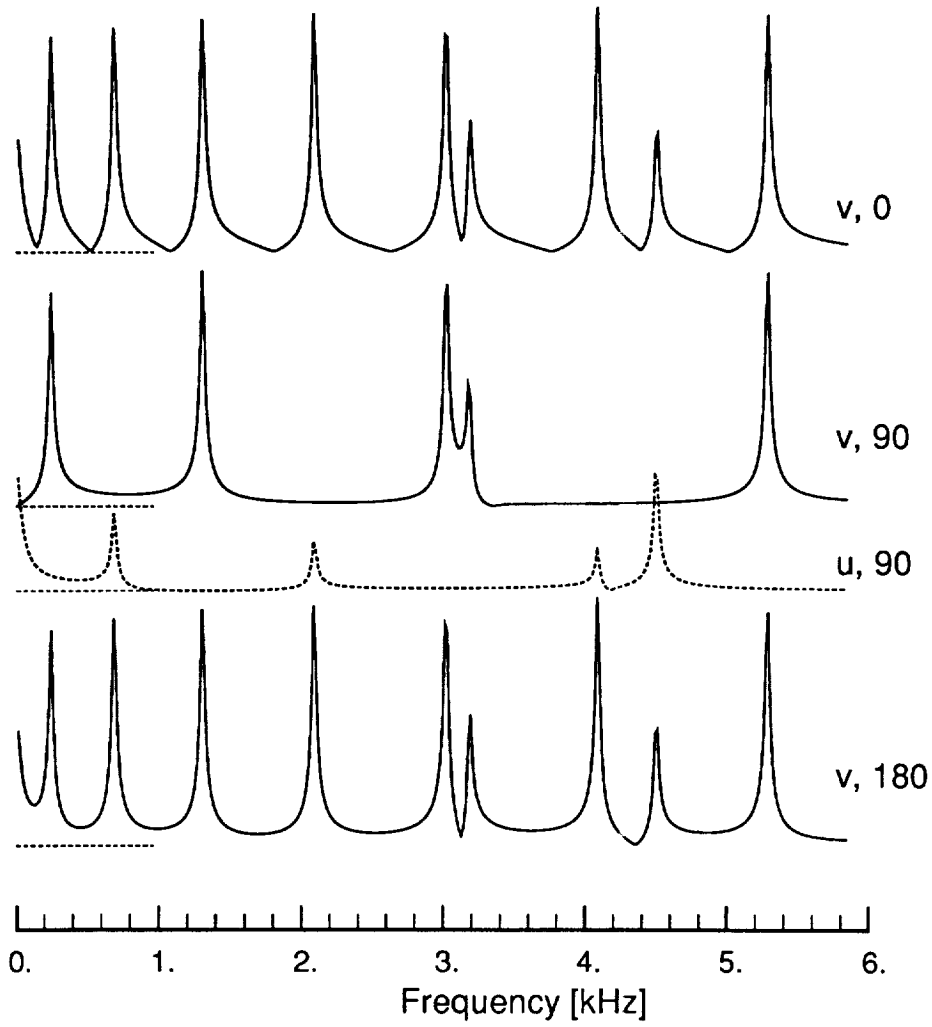

Figure 1.11: System response functions for the point excitation of a closed ring.

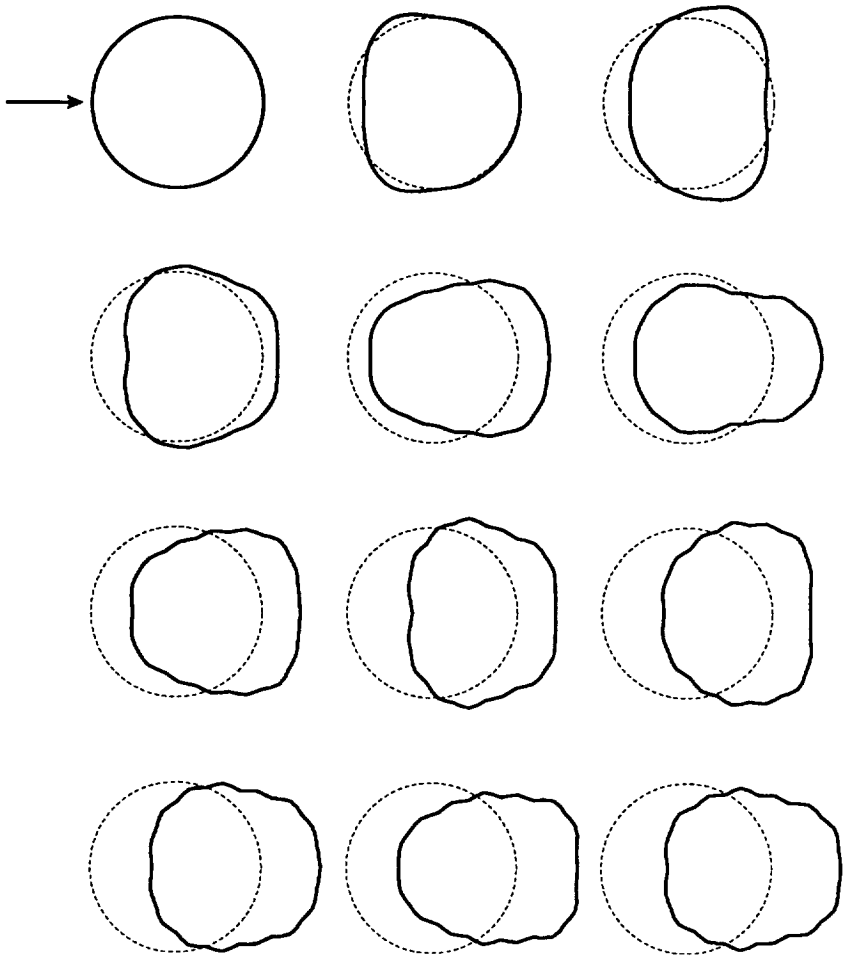

Figure 1.12: Deformed shapes (displacements scaled by 300) of a ring due to a point excitation. Time intervals are every 750 μs.

Chapter 2

Long Segmented Cylindrical Shells

The spectral element method for wave propagation in folded plate structures is extended to problems involving curved members. By combining these curved spectral elements with previously presented flat spectral elements, the dynamic response of geometrically complex structures can be determined. Of particular interest in this paper is the coupling that occurs naturally between the in-plane and transverse degrees of freedom and how it affects the element formulation. As an example of the utility of this element, the point excitation of an infinite curved shell and a closed cylinder is demonstrated.

2.1 Introduction

There is considerable intrinsic interest in waves in curved members because of their use in such structures as arches, containment vessels, aircraft fuselages, and ship hulls. Some idea of the range of applications is described by Gould (1988) and thorough treatments of their formulation are given by Leissa (1973) and Markus (1988).

A frequency domain matrix methodology for analyzing wave propagation in complex folded plate structures was developed by Rizzi and Doyle (1992), Danial and Doyle (1995), and Danial et al (1996). This paper is a continuation of those researches but now extended to include curved segmented shells. At present, we consider only circular uniform cylinders but the segments can be of arbitrary length in the hoop direction. (In this way it is different from the finite strip method described by Hinton et al (1995).) Two spectral elements are derived: a single noded semi-infinite throw-off element, and a finite length two-noded element. Both of these elements exactly model the distribution of mass and thus can be of any length.

A flat plate element has eight degrees of freedom (Danial et al, 1996) and the assembled $[8 \times 8]$ stiffness is achieved as a combination of two $[4 \times 4]$ elements plus a rotation matrix. But the curved element has all eight degrees of freedom coupled and hence we must tackle the stiffness matrix directly as an $[8 \times 8]$ system. This is too cumbersome to do explicitly; consequently, we lay out a computer based method for establishing the shape functions and subsequently, the stiffness matrix. This adds to the computational burden, but as compensation we get an approach that is conceptually simpler and helps to unify the special results established in the earlier references.

An interesting aspect of shells is the coupling that occurs between the in-plane and flexural degrees of freedom. Unlike folded plate modeling where the coupling between the degrees of freedom occurs only at attachment nodes, the curved shell segment possesses coupling at the level of the differential equations of motion. This results in a spectrum relation that is relatively complicated. Therefore a portion of this paper is devoted to discussing the spectrum relation in some detail.

While curved shell segments can be combined with flat elements to form geometrically complex structures, we will not emphasize that aspect of their use. Rather, we wish to focus specifically on some of the wave propagation aspects. We look at two variations of a closed cylinder problem. The first is used to verify the accuracy of the formulation while the second explores the nature of the wave reflections in the hoop direction.

2.2 Spectral Analysis of a Cylindrical Shells

There are a variety of statements of the governing equations for shells; to be consistent with the Danial et al (1996) paper, we briefly summarize the derivation. To this end, we find it most expedient to first specify the deformation, obtain the strain and kinetic energies, and then use Hamilton's principle to derive the equations of motion and the appropriate boundary conditions.

Consider the segment of cylindrical shell shown in Figure 2.1. The shell has a radius R, thickness h, and is considered long in the y-direction. The 3-D deformation is approximated as

$$\begin{aligned} \bar{u}(s,y,z) &\approx u(s,y) - z\left(\frac{\partial w}{\partial s} + \frac{u}{R}\right) \\ \bar{v}(s,y,z) &\approx v(s,y) - z\frac{\partial w}{\partial y} \\ \bar{w}(s,y,z) &\approx w(s,y) \end{aligned} \tag{2.1}$$

where $u(s,y)$ is the mean mid-plane circumferential displacement, $v(s,y)$ is the lengthwise displacement, and $w(s,y)$ is the radial displacement. This deformation leads to the non-zero strains

$$\begin{aligned} \epsilon_{ss} &= -\frac{w}{R} + \frac{\partial u}{\partial s} - z\left(\frac{\partial^2 w}{\partial s^2} + \frac{1}{R}\frac{\partial u}{\partial s}\right) \\ \epsilon_{yy} &= \frac{\partial v}{\partial y} - z\frac{\partial^2 w}{\partial y^2} \\ 2\epsilon_{sy} &= \frac{\partial v}{\partial s} + \frac{\partial u}{\partial y} - z\left(2\frac{\partial^2 w}{\partial s \partial y} + \frac{1}{R}\frac{\partial u}{\partial y}\right) \end{aligned} \tag{2.2}$$

Other shell theories have slightly different expressions for these strains; the present theory is closest to that of Reissner (1946) and Naghdi (1964). Excellent surveys of the different theories are given by Leissa (1973), and Markus (1988). The theory developed here is the shell equivalent of the classical plate theory and the Bernoulli-Euler beam theory.

An application of Hamilton's principle (Doyle, 1991) leads to the three governing equations of motion (for $R = constant$)

$$\begin{aligned} &\bar{E}[\frac{\partial^2 u}{\partial s^2} + \tfrac{1}{2}(1-\nu)\frac{\partial^2 u}{\partial y^2} + \tfrac{1}{2}(1+\nu)\frac{\partial^2 v}{\partial s \partial y} - \frac{1}{R}\frac{\partial w}{\partial s}] \\ &+\frac{1}{R^2}D[\frac{\partial^2 u}{\partial s^2} + \tfrac{1}{2}(1-\nu)\frac{\partial^2 u}{\partial y^2} + R(\frac{\partial^3 w}{\partial y^2 \partial s} + \frac{\partial^3 v}{\partial s^3})] = \rho h\frac{\partial^2 u}{\partial t^2} + \eta h\frac{\partial u}{\partial t} \\ &\bar{E}[\tfrac{1}{2}(1+\nu)\frac{\partial^2 u}{\partial s \partial y} + \frac{\partial^2 v}{\partial y^2} + \tfrac{1}{2}(1-\nu)\frac{\partial^2 v}{\partial s^2} - \frac{\nu}{R}\frac{\partial w}{\partial y}] = \rho h\frac{\partial^2 v}{\partial t^2} + \eta h\frac{\partial v}{\partial t} \end{aligned}$$

$$-\bar{E}[\frac{1}{R}\frac{\partial u}{\partial s}+\frac{\nu}{R}\frac{\partial v}{\partial y}-\frac{w}{R^2}] \tag{2.3}$$

$$+D[\frac{\partial^4 w}{\partial s^4}+2\frac{\partial^4 w}{\partial s^2\partial y^2}+\frac{\partial^4 w}{\partial y^4}]+\frac{1}{R}D[\frac{\partial^3 u}{\partial y^2\partial s}+\frac{\partial^3 u}{\partial s^3}] \;=-\rho h\frac{\partial^2 w}{\partial t^2}-\eta h\frac{\partial w}{\partial t}$$

where ν is Poisson's ratio, $D \equiv Eh^3/12(1-\nu^2)$, and $\bar{E} \equiv Eh/(1-\nu^2)$. We have added some viscous damping through the η terms.

Let the virtual work of the applied loads be

$$\delta V = -Q_u\delta u - Q_v\delta v - Q_w\delta w - Q_\psi\delta\psi\,, \qquad \psi \equiv \frac{\partial w}{\partial s}$$

then Hamilton's principle also gives the associated boundary conditions on the side $s = constant$ as:

$$\begin{aligned}
u \quad &\text{or} \quad Q_u = \bar{E}\left[\frac{\partial u}{\partial s}-\frac{w}{R}+\nu\frac{\partial v}{\partial y}\right]+\frac{1}{R}D\left[\frac{\partial^2 w}{\partial s^2}+\frac{1}{R}\frac{\partial u}{\partial s}+\nu\frac{\partial^2 w}{\partial y^2}\right]\\
v \quad &\text{or} \quad Q_v = \tfrac{1}{2}(1-\nu)\bar{E}\left[\frac{\partial v}{\partial s}+\frac{\partial u}{\partial y}\right]\\
w \quad &\text{or} \quad Q_w = \frac{1}{R}D\left[\frac{\partial^2 u}{\partial s^2}+(1-\nu)\frac{\partial^2 u}{\partial y^2}\right]-D\left[\frac{\partial^3 w}{\partial s^3}+(2-\nu)\frac{\partial^3 w}{\partial s\partial y^2}\right]\\
\psi = \frac{\partial w}{\partial s} \quad &\text{or} \quad Q_\psi = D\left[\frac{\partial^2 w}{\partial s^2}+\nu\frac{\partial^2 w}{\partial y^2}+\frac{1}{R}\frac{\partial u}{\partial s}\right]
\end{aligned} \tag{2.4}$$

We can form the resultants per unit length as

$$N_{ss} \equiv \int \sigma_{ss}\,dz\,, \qquad N_{sy} \equiv \int \sigma_{sy}\,dz\,, \qquad M_{ss} \equiv -\int \sigma_{ss} z\,dz\,, \qquad M_{sy} \equiv -\int \sigma_{sy} z\,dz$$

where the integrations are over the cross-section. After substituting for the stresses and strains in terms of our approximations, we get that the natural boundary conditions are equivalent to specifying

$$\begin{aligned}
Q_u &= N_{ss}+\frac{1}{R}M_{ss}\\
Q_v &= N_{sy}\\
Q_w &= -\frac{\partial M_{ss}}{\partial s}-2\frac{\partial M_{sy}}{\partial y} = V_{sz}\\
Q_\psi &= M_{ss}
\end{aligned} \tag{2.5}$$

The first of these resembles the resultant load expression used for curve beams (Bilodeau and Doyle, 1997), while the third resembles the Kirchhoff shear stress relation (Doyle, 1997).

Spectral analysis assumes solutions of the form

$$\boldsymbol{u}(s,y,t) = \sum_{n=1}^{N}\sum_{m=0}^{M}\tilde{u}(s,\omega_n,\xi_m)\,e^{-i\xi_m y}e^{i\omega_n t}\,, \qquad \xi_m = \frac{2\pi\,m}{W} \quad \omega_n = \frac{2\pi\,n}{T} \tag{2.6}$$

where W and T are the space and time windows, respectively. The use of these representation is documented by Danial and Doyle (1995). In this paper, we limit ourselves to problems that are symmetric about $y = 0$ and use $\cos(\xi_m y)$ with u and w, and use $\sin(\xi_m y)$ with v. When these are substituted into the governing differential equations, we get a set of ordinary differential equations with constant coefficients. These have solutions of the form

$$\tilde{u}(s,\omega,\xi) = u_o e^{-iks}, \qquad \tilde{v}(s,\omega,\xi) = v_o e^{-iks}, \qquad \tilde{w}(s,\omega,\xi) = w_o e^{-iks}$$

where $k = k(\omega,\xi)$ is the wavenumber. In this representation, the amplitudes u_o, v_o, w_o, and the wavenumber are as yet undetermined. On substitution, these lead to the homogeneous system of equations

$$\begin{bmatrix} \alpha_1 - [k^2 + (1-\nu)\xi^2]D/R^2 & -\gamma & [\bar{E} + (k^2+\xi^2)D]ik/R \\ \gamma & \alpha_2 & \nu\bar{E}\xi/R \\ [\bar{E} + (k^2+\xi^2)D]ik/R & -\nu\bar{E}\xi/R & \alpha_3 + \bar{E}/R^2 \end{bmatrix} \begin{Bmatrix} u_o \\ v_o \\ w_o \end{Bmatrix} = 0 \qquad (2.7)$$

using

$$\begin{aligned} \alpha_1 &\equiv -\bar{E}[k^2 + \tfrac{1}{2}(1-\nu)\xi^2] + \rho h\bar{\omega}^2, \quad \gamma \equiv \tfrac{1}{2}(1+\nu)\bar{E}ik\xi \\ \alpha_2 &\equiv -\bar{E}[\xi^2 + \tfrac{1}{2}(1-\nu)k^2] + \rho h\bar{\omega}^2, \quad \alpha_3 \equiv D[k^2+\xi^2]^2 - \rho h\bar{\omega}^2 \end{aligned}$$

and $\bar{\omega}^2 \equiv \omega^2 - i\omega\eta/\rho$. The α_1, α_2 and γ terms alone define the flat membrane problem, while α_3 alone defines the flat plate flexural problem. All the other terms are couplings. For a non-trivial solution, the determinant must be zero and this allows k to be determined. This has eight solutions in all, but since only k^2 terms appear, there are four basic modes appearing as $\pm k_j$ pairs.

For each wavenumber k_j, Equation (2.7) gives the relation among the amplitudes. This is homogeneous and therefore, at best, we can only get amplitude ratios. For example, we can solve for the remaining two terms as a function of u_o. In anticipation of a later need, we add $\psi_o = -ikw_o$ and write the solutions at a particular wavenumber k_j as

$$\begin{Bmatrix} u_o \\ v_o \\ w_o \\ \psi_o \end{Bmatrix}_j = \begin{Bmatrix} 1 \\ \Phi_v \\ \Phi_w \\ \Phi_\psi \end{Bmatrix}_j u_o = \{\Phi\}_j u_o$$

where the symbol Φ indicates an amplitude ratio. Although the vector $\{\Phi\}$ shown is normalized with respect to u_o, it is possible for other modal vectors to be normalized differently. This must be done for each mode k_j and hence there are eight vectors.

We choose to represent these as $[\ \Phi\ ] = [[\Phi_A], [\Phi_B]]$ where

$$[\Phi_A] \equiv \left[\begin{Bmatrix} 1 \\ \Phi_v \\ \Phi_w \\ \Phi_\psi \end{Bmatrix}_1 \begin{Bmatrix} \Phi_u \\ 1 \\ \Phi_w \\ \Phi_\psi \end{Bmatrix}_2 \begin{Bmatrix} \Phi_u \\ \Phi_v \\ 1 \\ \Phi_\psi \end{Bmatrix}_3 \begin{Bmatrix} \Phi_u \\ \Phi_v \\ 1 \\ \Phi_\psi \end{Bmatrix}_4 \right]$$

and $[\Phi_B]$ is the same but evaluated at the wavenumbers $-k_j$. That is, the $[4 \times 4]$ partitions $[\Phi_A]$ and $[\Phi_B]$ are evaluated at $+k_j$ and $-k_j$, respectively; they are fully populated and typically are not symmetric. The normalizations are arranged so that the uncoupled flat plate solutions are easily recovered.

For each mode, the corresponding amplitude u_{oj} is undetermined; to make the notation resemble what we have already used, we will label each of the these $\mathbf{A}$, $\mathbf{B}$, $\cdots$. The solution for the displacements can then be expressed as

$$\tilde{u}(s) \;=\; \mathbf{A}\Phi_{11}e^{-ik_1 s} + \mathbf{B}\Phi_{12}e^{-ik_2 s} + \cdots + \mathbf{G}\Phi_{17}e^{+ik_3 s} + \mathbf{H}\Phi_{18}e^{+ik_4 s} \qquad (2.8)$$

with similar expressions for $\tilde{v}$, $\tilde{w}$, and $\tilde{\psi}$, but involving the amplitude ratios Φ_{2j}, Φ_{3j}, and Φ_{3j}, respectively. The coefficients $\mathbf{A}, \mathbf{B}, \cdots, \mathbf{H}$ are to be determined from the boundary conditions.

It is apparent that the spectrum relation $k(\omega, \xi)$ plays a central role in the solution, and since the characteristic equation is rather complicated, we look at its solution in greater detail next.

2.3 Discussion of the Spectrum Relations

The characteristic equation to determine the wavenumber $k(\omega, \xi)$ is formed by setting the determinant of system (2.7) to zero. On expansion, we find the characteristic equation can be rearranged as

$$k^8 + A_3 k^6 + A_2 k^4 + A_1 k^2 + A_0 = 0 \tag{2.9}$$

The expressions for the coefficients A_n are too complicated to be listed here. This has eight solutions in all, but since only k^2 terms appear, there are four basic modes appearing as $\pm k_j$: two associated with the in-plane behavior and two associated with the flexural behavior. In general, of course, the modes are coupled and it is not proper to speak of a membrane mode or a flexural mode.

We must solve a quartic equation in order to get the full behavior of the spectrum relations. While the formulas for doing this are relatively straight-forward, they cause some difficulties which are worth discussing.

Following Abramowitz and Stegan (1965), we first write the characteristic equation as the conjugate factorization for $z = k^2$

$$\left[z^2 + (a+b)z + (c+d)\right]\left[z^2 + (a-b)z + (c-d)\right] = 0$$

This allows z to be determined from a sequence of quadratic equations. The coefficients appearing in the above are

$$a = \tfrac{1}{2}A_3\,, \qquad b = \tfrac{1}{2}\sqrt{8c + A_3^2 - 4A_2}\,, \qquad d = \sqrt{c^2 - A_0}$$

and c is chosen as a solution of the cubic equation

$$c^3 - \tfrac{1}{2}[A_2]c^2 + \tfrac{1}{4}[A_1 A_3 - 4A_0]c + \tfrac{1}{8}[A_0 A_3^2 + A_1^2 - 4A_0 A_2] = 0$$

The formulas to solve the cubic equation are based on those of Abramowitz and Stegan (1965) and Press et al (1992). We first write the equation as

$$c^3 + a_2 c^2 + a_1 c + a_0 = 0$$

and then compute the terms

$$q = (a_2^2 - 3a_1)/9\,, \qquad r = (2a_2^3 - 9a_2 a_1 + 27a_0)/54\,, \qquad s_{1,2} = -[r \pm \sqrt{r^2 - q^3}]^{1/3}$$

The three roots for c are then given by

$$\begin{aligned} c_1 &= (s_1 + s_2) - \tfrac{1}{3}a_2 \\ c_2 &= -\tfrac{1}{2}(s_1 + s_2) - \tfrac{1}{3}a_2 + i\tfrac{1}{2}(s_1 - s_2)\sqrt{3} \\ c_3 &= -\tfrac{1}{2}(s_1 + s_2) - \tfrac{1}{3}a_2 - i\tfrac{1}{2}(s_1 - s_2)\sqrt{3} \end{aligned}$$

The eight spectrum relations are given as $\pm\sqrt{z}$.

These equations can be easily programmed. The difficulty that arises is in choosing the appropriate square or cube root in both the cubic and quadratic solvers, as well as the appropriate root from the cubic solver. It is seen that while there are only four z roots, the formulas give a multiplicity of 144 roots. This is especially acute since we wish to compute a single z_j at a time. The issue is that in computing the n^{th} root of a complex number $z = a + ib = Ae^{i\phi}$, the phase $\phi = \tan^{-1}(b/a)$ has an ambiguity of $N\pi$.

We remove this ambiguity by keeping track of the total phase. That is, starting with some value and with reference to the unit circle in the complex plane, as the wavenumber goes from the 4^{th} to the 1^{st} quadrant the total phase is increased by 2π. Algorithmically, we compute complete modes separately at each m. Starting at a large value of frequency, we work toward the lower frequencies, keeping track of the phases. The root c is chosen as the one that had the largest real value initially. Approximate spectrum relations are useful here in identifying the appropriate modes. This scheme works quite robustly when the frequency decrement is not too large. Periodic checks with an iterative root finder helps confirm the correctness of the roots. It must be said that determining the spectrum relations is now a significant operation in itself, and unlike the previous reported cases, they are no-longer computed on-the-fly as part of the structural analysis.

An idea of the variety of behaviors is shown in Figure 2.2 for a value of $\xi = 2\pi m/W$ with $m = 40$. In this and the remaining examples, we consider an aluminum shell that is $25.4\,mm$ $(1.0\,in)$ thick with a radius of curvature, $R = 254\,mm$ $(10.0\,in)$. Also, we take $W = 20\,m$ $(800\,in)$. Using these values, the curvature has a significant effect on the spectrum relations. The figure shows for the first four spectrum relations; these correspond to propagating waves, and are characterized by a negative imaginary component.

Not surprising, there are many branch points in the spectrum relations. We clearly see three cut-off frequencies but what is interesting is that two of them are associated with k_2, the in-plane shear dominated mode. Note that both k_2 and k_4 have a negative real component at low frequencies and it might therefore be thought that this violates the radiation condition for waves propagation in the positive direction. In our approach, the wavenumbers always have an imaginary component — even predominantly real-only modes such as k_3 have an imaginary component arising from the damping. Thus the identification criterion is based on dissipation of energy in the positive direction. A negative real component is expected to lead to a standing

wave.

It is difficult to get a clear idea of the complete (i.e., as m varies) spectrum relations from Figure 2.2, it is useful, therefore, to introduce an approximation that will help to delineate the separate contributions. An approximation that is reasonable for thin shells of large radius is given by

$$\begin{aligned} k_1^2 &= k_P^2 - \frac{1}{R^2} - \xi^2 & k_3^2 &= \frac{1}{2R^2} - \xi^2 + \sqrt{k_B^4 + \frac{1}{4R^4} - \frac{\xi^2}{R^2}} \\ k_2^2 &= k_S^2 - \xi^2 & k_4^2 &= \frac{3}{2R^2} - \xi^2 - \sqrt{k_B^4 + \frac{9}{4R^4} - \frac{\xi^2}{R^2}} \end{aligned} \tag{2.10}$$

where $k_P^2 \equiv \omega^2\rho(1-\nu^2)/E$, $k_S^2 \equiv \omega^2\rho 2(1+\nu)/E$, and $k_B^4 \equiv \omega^2\rho h/D$. The first two are the membrane dominated modes and recover the plots shown in Rizzi and Doyle (1992) when R is very large. The third and fourth modes are the flexural dominated modes and for large R they recover the flat plate spectrum relations given by Doyle (1997). In comparison to the uncoupled modes, the major effect of the curvature is in the longitudinally dominated modes because the cut-off frequencies are affected and hence delay the formation of real-only wavenumbers.

Since the spectrum relations are relatively insensitive to R at large frequency, Then these approximations are quite useful in identifying the modes as determined by the root solver.

2.4 Spectral Element Formulation

When the number of degrees of freedom is large, we need an organized way to handle establishing the shape functions and the element stiffness. The cylindrically curved shell segment is such a case and we take this opportunity to develop an appropriate matrix scheme.

Consider a segment of shell of length L in the hoop direction. We begin by expressing the displacements as

$$\tilde{u}(s) = \mathbf{A}\Phi_{11}e^{-ik_1 s} + \mathbf{B}\Phi_{12}e^{-ik_2 s} + \cdots + \mathbf{G}\Phi_{17}e^{-ik_3(L-s)} + \mathbf{H}\Phi_{18}e^{-ik_4(L-s)} \quad (2.11)$$

with similar expressions for $\tilde{v}$, $\tilde{w}$, and $\tilde{\psi}$. The length is introduced to include reflections coming from a boundary located at $s = L$. This displacement solution can be re-written as

$$\begin{aligned} \{\tilde{u}(s),\, \tilde{v}(s),\, \tilde{w}(s),\, \tilde{\psi}(s)\}^T &= \{\mathcal{U}\}(s) \\ &= \{\Phi\}_1 \mathbf{A}e^{-ik_1 s} + \cdots + \{\Phi\}_8 \mathbf{H}e^{-ik_4(L-s)} \end{aligned}$$

We will re-write this in an even more compact matrix form; so as to make the matrix notation more accessible, we will take the developments of the rod as the archetype and use its notation (except changed to matrices). The 1-D solution for a rod is represented by Doyle (1997) as

$$\hat{u}(x) = [e^{-ik_1 x}]\mathbf{A} + [e^{-ik_1(L-x)}]\mathbf{B}$$

where **A** and **B** are associated with the forward moving and backward moving waves, respectively. The displacement for the shell segment is written as

$$\{\mathcal{U}\}(s) = [\Phi_A]\lceil e(s)\rfloor\{\mathbf{A}\} + [\Phi_B]\lceil e(L-s)\rfloor\{\mathbf{B}\}$$

were $[\Phi_A]$ or $[\Phi_B]$ are the $[4 \times 4]$ partitions of $[\ \Phi\ ]$ and

$$\lceil e(s)\rfloor \equiv \begin{bmatrix} e^{-ik_1 s} & 0 & 0 & 0 \\ 0 & e^{-ik_2 s} & 0 & 0 \\ 0 & 0 & e^{-ik_3 s} & 0 \\ 0 & 0 & 0 & e^{-ik_4 s} \end{bmatrix}, \qquad \{\mathbf{A}\} \equiv \begin{Bmatrix} \mathbf{A} \\ \mathbf{B} \\ \mathbf{C} \\ \mathbf{D} \end{Bmatrix}, \qquad \{\mathbf{B}\} \equiv \begin{Bmatrix} \mathbf{E} \\ \mathbf{F} \\ \mathbf{G} \\ \mathbf{H} \end{Bmatrix}$$

We wish to replace the vectors $\{\mathbf{A}\}$ and $\{\mathbf{B}\}$ in terms of the nodal displacements at $s = 0$ and $s = L$. That is, we introduce

$$\tilde{u}(0) = \tilde{u}_1\,, \quad \tilde{v}(0) = \tilde{v}_1\,, \quad \tilde{w}(0) = \tilde{w}_1\,, \quad \tilde{\psi}(0) = \tilde{\psi}_1$$

with similar, but subscripted '2', terms at $s = L$. We write this in matrix notation as

$$\begin{aligned}\{\tilde{u}_1, \tilde{v}_1, \tilde{w}_1, \tilde{\psi}_1\}^T = \{\tilde{u}\}_1 = \{\mathcal{U}\}(s=0) &= [\Phi_A]\lceil e(0)\rfloor\{\mathbf{A}\} - [\Phi_B]\lceil e(L)\rfloor\{\mathbf{B}\} \\ \{\tilde{u}_2, \tilde{v}_2, \tilde{w}_1, \tilde{\psi}_2\}^T = \{\tilde{u}\}_2 = \{\mathcal{U}\}(s=L) &= [\Phi_A]\lceil e(L)\rfloor\{\mathbf{A}\} - [\Phi_B]\lceil e(0)\rfloor\{\mathbf{B}\}\end{aligned}$$

Solving for the coefficients gives

$$\begin{Bmatrix}\{\mathbf{A}\} \\ \{\mathbf{B}\}\end{Bmatrix} = [\,G\,]\begin{Bmatrix}\{\tilde{u}\}_1 \\ \{\tilde{u}\}_2\end{Bmatrix} = \begin{bmatrix}[G_{11}] & [G_{12}] \\ [G_{21}] & [G_{22}]\end{bmatrix}\begin{Bmatrix}\{\tilde{u}\}_1 \\ \{\tilde{u}\}_2\end{Bmatrix}$$

where each partition of $[\,G\,]$ is of size $[4 \times 4]$. We are now in a position to write the displacements in terms of the shape functions. They are

$$\{\mathcal{U}\}(s) = [g(s)]_1\{\tilde{u}\}_1 + [g(s)]_2\{\tilde{u}\}_2 \tag{2.12}$$

where the $[4 \times 4]$ matrix of shape functions are defined as

$$\begin{aligned}[g(s)]_1 &= [\Phi_A]\lceil e(s)\rfloor[G_{11}] + [\Phi_B]\lceil e(L-s)\rfloor[G_{21}] \\ [g(s)]_2 &= [\Phi_A]\lceil e(s)\rfloor[G_{12}] + [\Phi_B]\lceil e(L-s)\rfloor[G_{22}]\end{aligned} \tag{2.13}$$

There are a total of $4 \times 4 \times 2 = 32$ shape functions. While not obvious from the above, it turns out that, even in this general case, the collection of shape functions associated with the degrees of freedom at the second node are the mirror image of those associated with the degrees of freedom at the first node. The results for the throw-off element are simply are simply those associated with $[G_{11}]$. These formulas can be used to recover all the shape functions already derived in the cited references.

By way of example, Figure 3.6 shows the $g_{33}(s)\cos(\xi_m y)$ shape function of a 270^o shell segment; this shape function is associated with the $\tilde{w}_1$ degree of freedom and thus can be plotted as a radial displacement off the original shape. These shape functions are similar in concept to conventional finite element shape functions except that they are frequency and wavenumber dependent, are typically complex, and can represent the behavior of very large segments. The other shape functions behave in a similar manner. It is clear from this figure and from the above developments, that once the nodal degrees of freedom are determined then the shape functions can be used to compute the responses at any intermediate locations. This is a crucial attribute since the segments can be very large.

The next step in the element development is to derive a stiffness relation for the shell segment. The process is simply that of expressing the resultant forces and moments from Equation (2.5) in terms of the displacement solutions given in Equation (2.12). We write these resultants in matrix form as

$$\{\mathcal{F}\}(s) = \{N_{ss} + \frac{1}{R}M_{ss},\, N_{sy},\, V_{sz},\, M_{ss}\}^T(s) = [\,\partial\,]\{\mathcal{U}\}(s)$$

where [∂] is the matrix collection of differential operators of size [4 × 4]. After substituting for $\{\mathcal{U}\}(s)$ in terms of the shape functions get

$$\begin{aligned}\{\mathcal{F}\}(s) &= [\ \partial\ ][g(s)]_1\{\tilde{u}\}_1 + [\ \partial\ ][g(s)]_2\{\tilde{u}\}_2 \\ &\equiv [\partial g(s)]_1\{\tilde{u}\}_1 + [\partial g(s)]_2\{\tilde{u}\}_2 \end{aligned} \tag{2.14}$$

Relating the member resultants at $s = 0$ and $s = L$ to the nodal loads at the same locations leads to the stiffness relation

$$\begin{Bmatrix} \{\tilde{F}\}_1 \\ \{\tilde{F}\}_2 \end{Bmatrix} = \begin{bmatrix} [-\partial g(0)]_1 & [-\partial g(0)]_2 \\ [+\partial g(L)]_1 & [+\partial g(L)]_2 \end{bmatrix} \begin{Bmatrix} \{\tilde{u}\}_1 \\ \{\tilde{u}\}_2 \end{Bmatrix} \tag{2.15}$$

or simply $\{\tilde{F}\} = [\tilde{k}(\omega,\xi)]\{\tilde{u}\}$ where

$$\{\tilde{F}\} = \{\tilde{N}_1,\ \tilde{F}_{y_1},\ \tilde{V}_1,\ \tilde{M}_1;\ \tilde{N}_2,\ \tilde{F}_{y_2},\ \tilde{V}_2,\ \tilde{M}_2\}^T, \quad \{\tilde{u}\} \equiv \{\tilde{u}_1,\ \tilde{v}_1,\ \tilde{w}_1,\ \tilde{\psi}_1;\ \tilde{u}_2,\ \tilde{v}_2,\ \tilde{w}_2,\ \tilde{\psi}_2\}^T$$

and [$\tilde{k}$] is the [8 × 8] dynamic element stiffness matrix. This stiffness matrix is frequency and wavenumber dependent, complex, and symmetric. The stiffness relation for the throw-off or one-noded element is simply

$$\{\tilde{F}\}_1 = [-\partial g(0)]_1\{\tilde{u}\}_1 = [\tilde{k}(\omega,\xi)]\{\tilde{u}\}_1 \tag{2.16}$$

The stiffness matrix in this case is of size [4 × 4]. These stiffness relations can be used to recover the results already presented in the cited references.

For illustrative purposes, Figure 2.4 shows the normalized $\tilde{k}_{11}$, $\tilde{k}_{22}$, $\tilde{k}_{33}$, and $\tilde{k}_{44}$ diagonal terms for the same shell used to illustrate the shape functions. As is typical with spectral elements, they exhibit a very large dynamic range. The normalizations are with respect to the stiffnesses for straight thin beams (Doyle, 1991) but modified for plates. That is, they are presented as

$$\tilde{k}_{11}/(Eh/L)\,, \qquad \tilde{k}_{22}/(Gh/L)\,, \qquad \tilde{k}_{33}/(12D/L^3)\,, \qquad \tilde{k}_{44}/(4D/L)$$

Note that the $\tilde{k}_{11}$ stiffness is substantially less than the static values, and it is only after the cut-off frequency ($\approx 3\,kHz$ for $m = 0$) does it become greater than unity. On the other hand, $\tilde{k}_{33}$ is always significantly larger than the static straight value; this is because the L^3 in the denominator predicts an inordinately small static value.

2.5 Point Excitation of a Shell

The advantage of the curved element is that it can be combined with other elements — either flat or curved — to form significantly more complex structures. Danial and Doyle (1994, 1995) discuss aspects of the computer programming structure required for multiply connected spectral elements; they also show how the spectral element method can be hosted on a massively parallel machine. The variety of possibilities is too great to pursue here, so we will be content with two short examples. Both involve the point excitation of a complete cylindrical shell but the latter shifts the boundaries so as to explore the nature of the reflections.

We form the complete cylinder by combining two curved elements of the same material properties each of which is a half-circle. Because of symmetry, we could model the shell with a single half-circle element or as a single whole-circle element. In the latter case, half of the applied load must be placed at each node and the extra conditions of $\tilde{u}_1 = 0$, $\tilde{\psi}_1 = 0$; $\tilde{u}_2 = 0$, $\tilde{\psi}_2 = 0$ be imposed. The two element model was chosen so as to verify the assemblage process.

The elements can be joined at the common nodes by merely summing together the appropriate dynamic stiffness matrix components to form a global stiffness matrix $[\hat{K}]$. We must therefore first rotate each element stiffness to this global system. This must take into account that the ends of the curved element are oriented differently to each other and an appropriate scheme is illustrated by Bilodeau and Doyle (1997). The global stiffness matrix is then simply formed by adding the two global element stiffness matrices together.

With the elements connected, we can now determine the responses due to a point excitation. The input force history used is the same as used by Danial et al (1996): it is a pulse of duration of about $120\,\mu s$, and has a frequency content of about $16\,kHz$. The velocity reconstructions for three points, $\theta = 0^o$, 90^o, 180^o, along the circumference are shown in Figure 2.5. For comparison purposes, the same shell was modeled using 64 flat spectral elements. The two sets of results are indistinguishable even though there are very many reflections. It is worth pointing out that when fewer flat elements were used the results deteriorated as the time increased. This shows the significant computational savings in using the curved element.

There are obvious multiple reflections occurring. The waves travel around the circumference and interact with each other. We can get an alternative insight by looking at the system response function $\hat{G}$ where $\hat{u} = \hat{G}\hat{P}$ and $\hat{P}$ is the input load. Note that this facility is an integral attribute of the spectral element formulation.

From Figure 2.6, we can see that many resonance frequencies are being established. These would be the frequencies of interest if an impulse/modal analysis experiment vibration experiment were being performed. It is interesting to note that the w response at 0^o and 180^o exhibit similar resonant behavior, but the response at 90^o is missing many of the intermediate resonances. A significant peak appears at about $3.3\,kHz$; we now look further at this.

We wish to explore the effect of the reflections on the formation of the spectral peaks. To do this, we will model the cylinder as a sequence of increasing elements but of the same radius — the cylinders can be viewed as forming helical coils. The net effect is to place Node 2 further and further away from Node 1. The final model is a single throw-off element. We use the same broad band excitation and the velocity reconstructions are shown in Figure 3.2. There are two points of interest. First, note how all traces have the same initial behavior — this is the duration before any reflections return. The 180^o element shows the most reflections and these diminish with increasing element size. The second point of note the trailing oscillatory behavior even for the infinite element. Although the force excitation lasts less than $200\,\mu s$, the plate continues to oscillate in an almost resonant like fashion. Actually, a standing wave has been established.

A different view of these behaviors is obtained by looking at the velocity responses in the frequency domain. It is clear in Figure 2.8 that there is the formation of an increasing number of spectral peaks as the element length is increased. This is expected but what is interesting is a peak in the w-velocity response in the infinite length case. An analysis of the amplitude ratios shows that this peak is coming entirely from the first mode even though the response overall is dominated by the first mode. What is happening is that the curvature acts effectively as a continuous boundary and sets up a standing wave.

The flexibility of the spectral element approach has allowed us to view the problem of the impact of a cylinder as one of wave propagation or vibration. This comes about because of the convenience in alternating between the time and frequency domains.

2.6 Discussion

A spectral shell element was developed that extends the variety of problems the spectral element method can handle. It was shown to be accurate and certainly more computationally efficient than using multiple flat plate elements. The element developed possesses all of the features of the spectral element method which make the method desirable for solving dynamic problems. Primary among these are that the element can be very long and that the frequency domain formulation allows the system response functions to be determined automatically. This latter attribute, along with the fast Fourier transform, enables a duality between the time domain and frequency domain to be presented conveniently. Information not readily seen in one is often detectable in the other. The example problems demonstrate these features.

One of the challenges that arose during the development was the problem of determining the spectrum relations. Even though formulas for the solution of quartic equations were derived, it is not always certain which branch should be chosen after a branch point occurs. In the quadratic case, which occurs for flat plates, the ambiguity is removed by adding damping. This becomes essential in the general case so that the phase of each $k_j(\omega, \xi)$ can be tracked correctly — the effect of the damping is to separate each of the modes. The damping is also necessary in order to distinguish between the forward and backward moving waves.

Based on the problems we have considered, it is clear that once there is more than one connection in a structure, it is essential to have a matrix methodology to handle the many unknowns. The spectral element approach presents itself as a well founded matrix method that embodies a number of efficiencies we have long associated with the conventional finite element method. For the range of problems they are suited for, they show great efficiencies and conveniences. Being formulated in the frequency domain means it is also ideally suited for energy flow analysis of the type described by Langley (1994). It is also appropriately formulated for tackling the solid/fluid interaction problems as occur in structural acoustics. A beginning in this direction is described by Bilodeau (1995).

The approach as presented so far has difficulty with localized discontinuities of properties or geometry unless the have a very simple geometry. At present, there is also the restriction that lateral boundaries must be relatively far away. Similarly, there is a restriction that the material properties and geometry in the lateral direction be uniform. It is hoped to tackle these issues in the future.

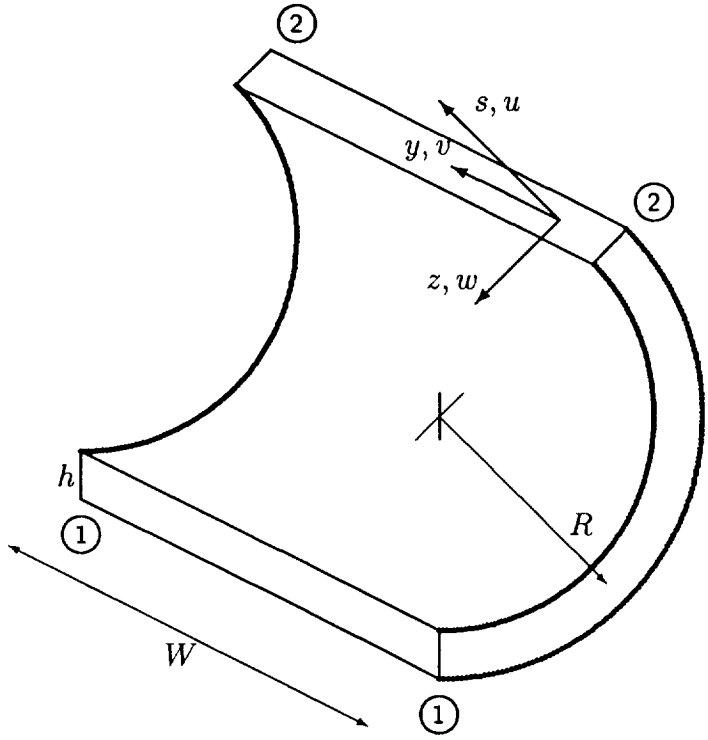

Figure 2.1: Coordinate system and displacements for a segment of cylindrical shell.

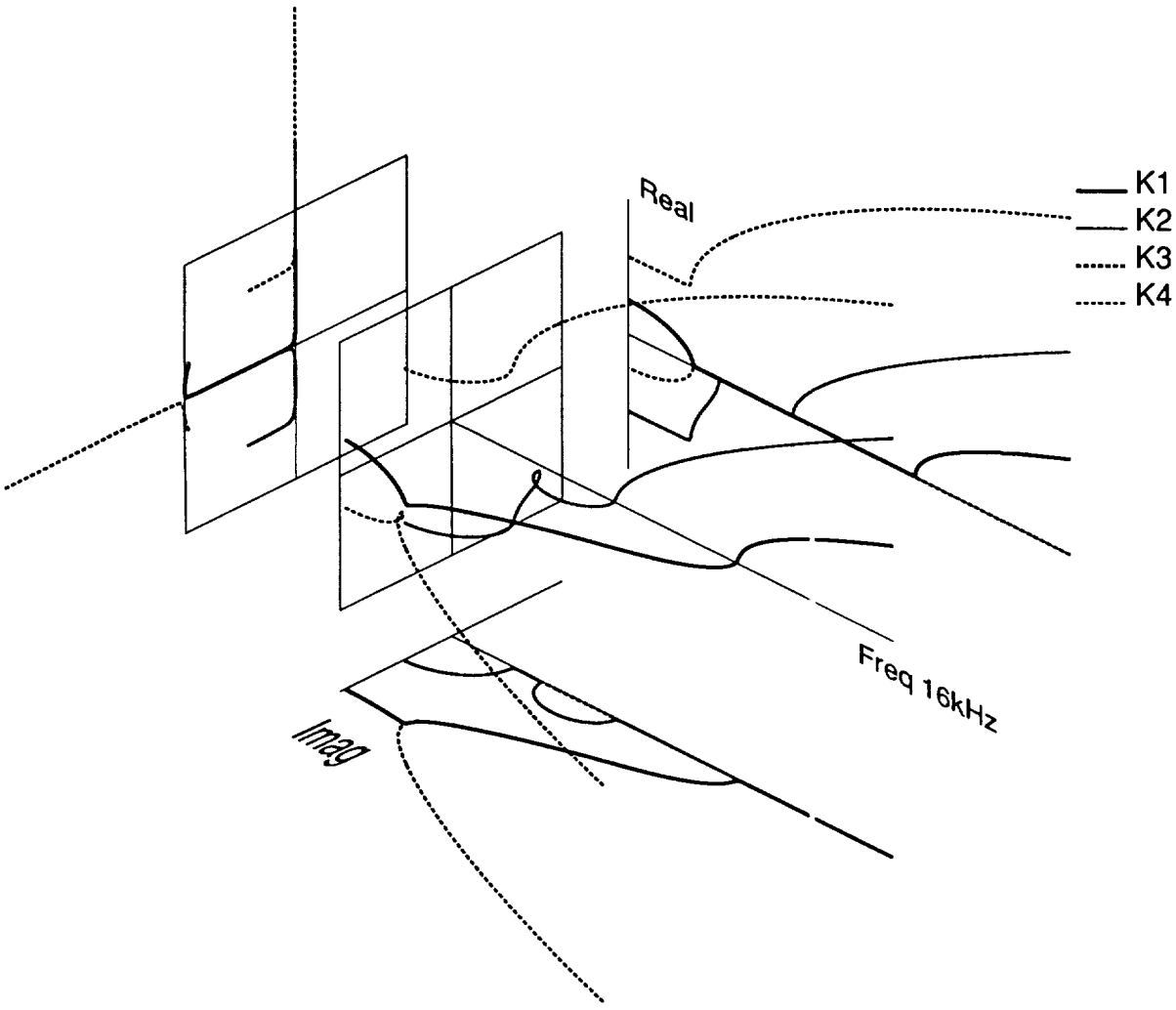

Figure 2.2: Spectrum relations $k_j h$ for a shell segment with $R = 254\,mm$ and $h = 25.4\,mm$, and $m = 40$.

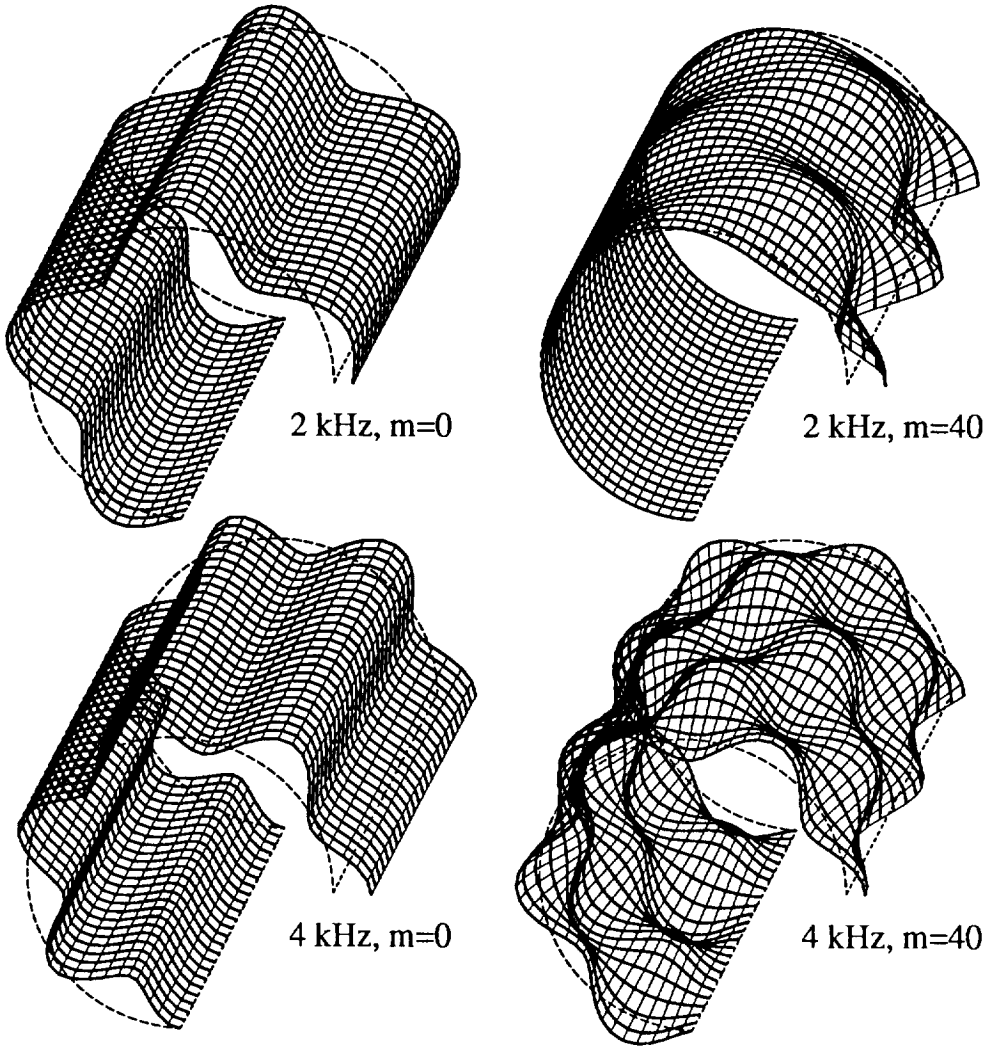

Figure 2.3: Samples of shape functions for a 270^o shell segment.

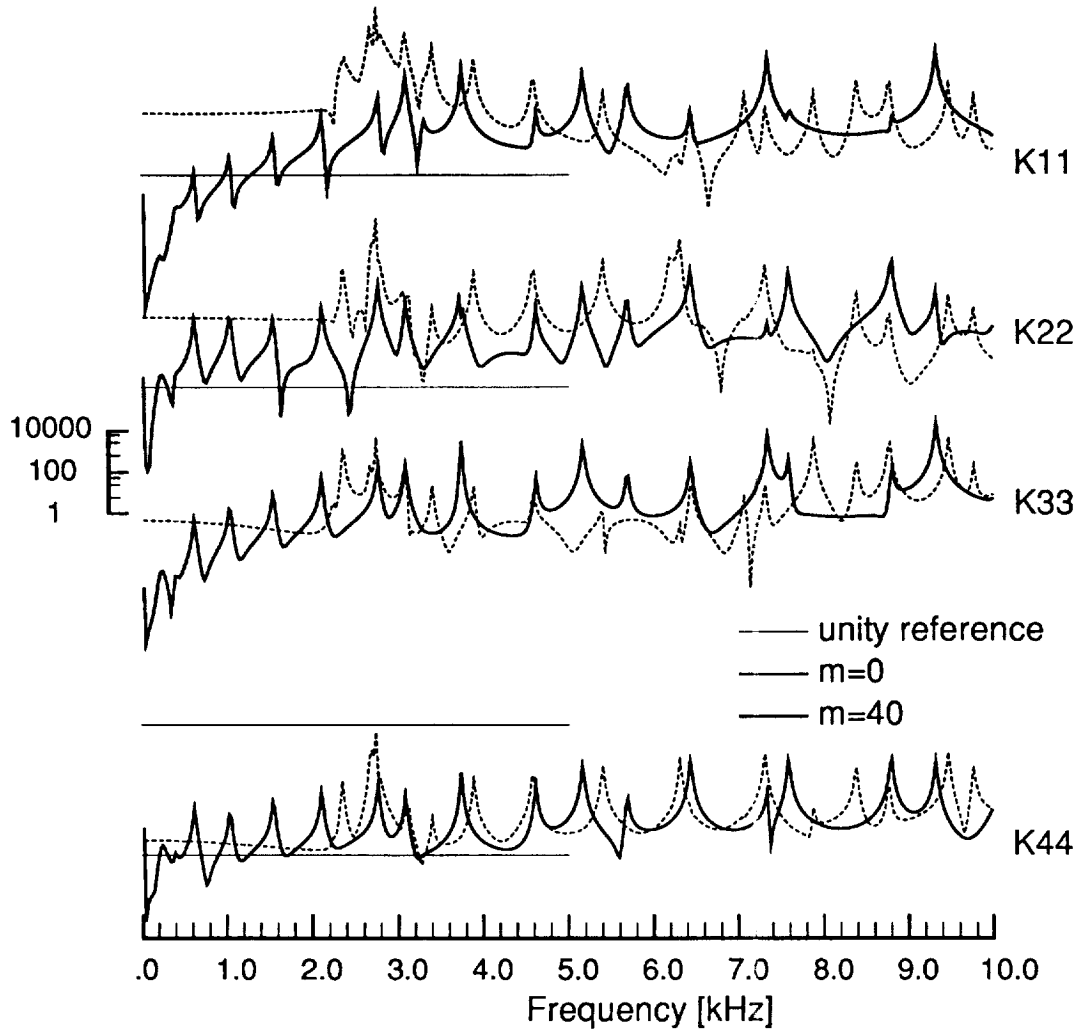

Figure 2.4: Normalized stiffnesses $\hat{k}_{11}$, $\hat{k}_{22}$, $\hat{k}_{33}$, and $\hat{k}_{44}$ for a 270^o shell segment.

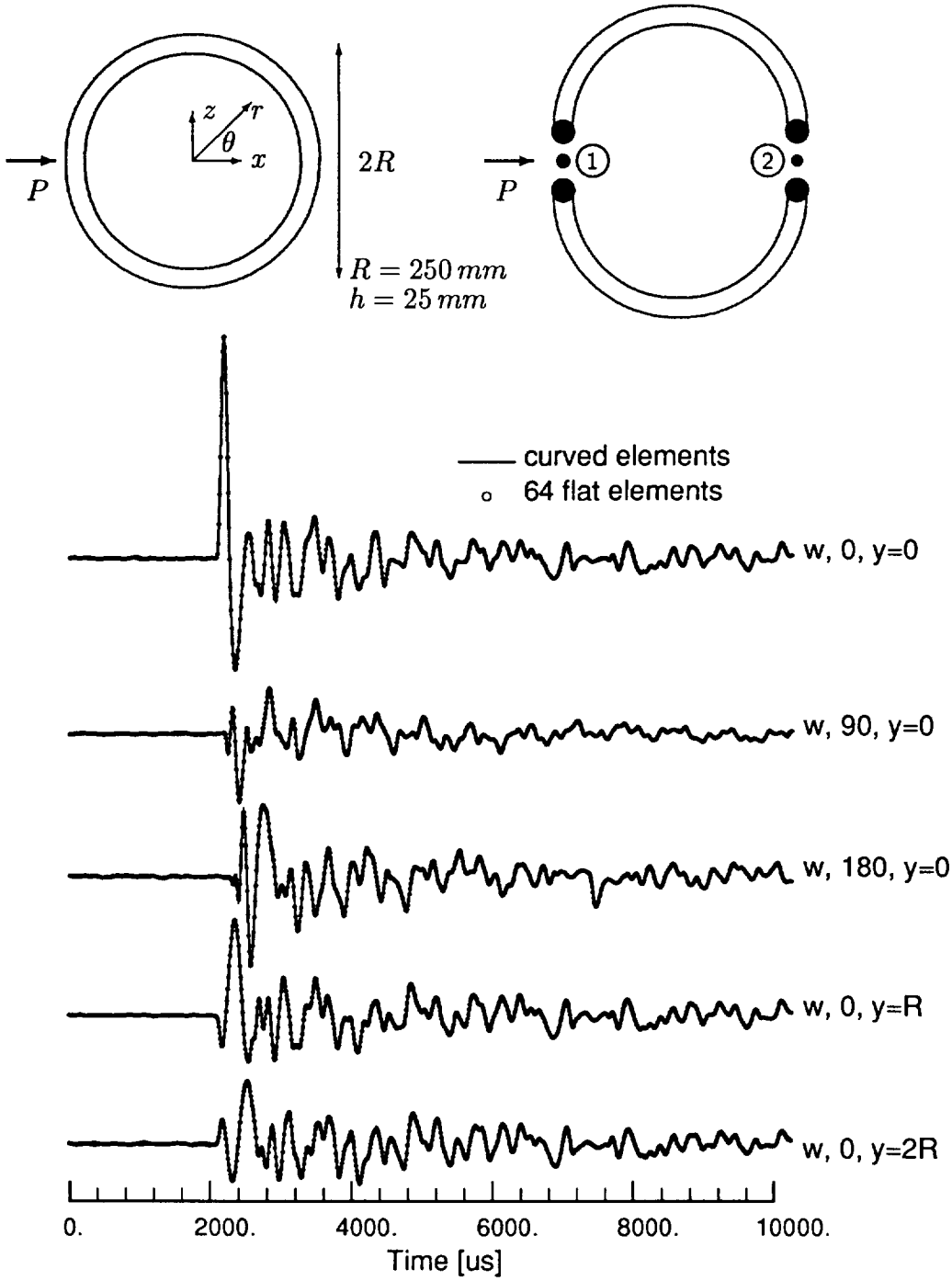

Figure 2.5: Velocity reconstructions for the point excitation of a closed cylinder.

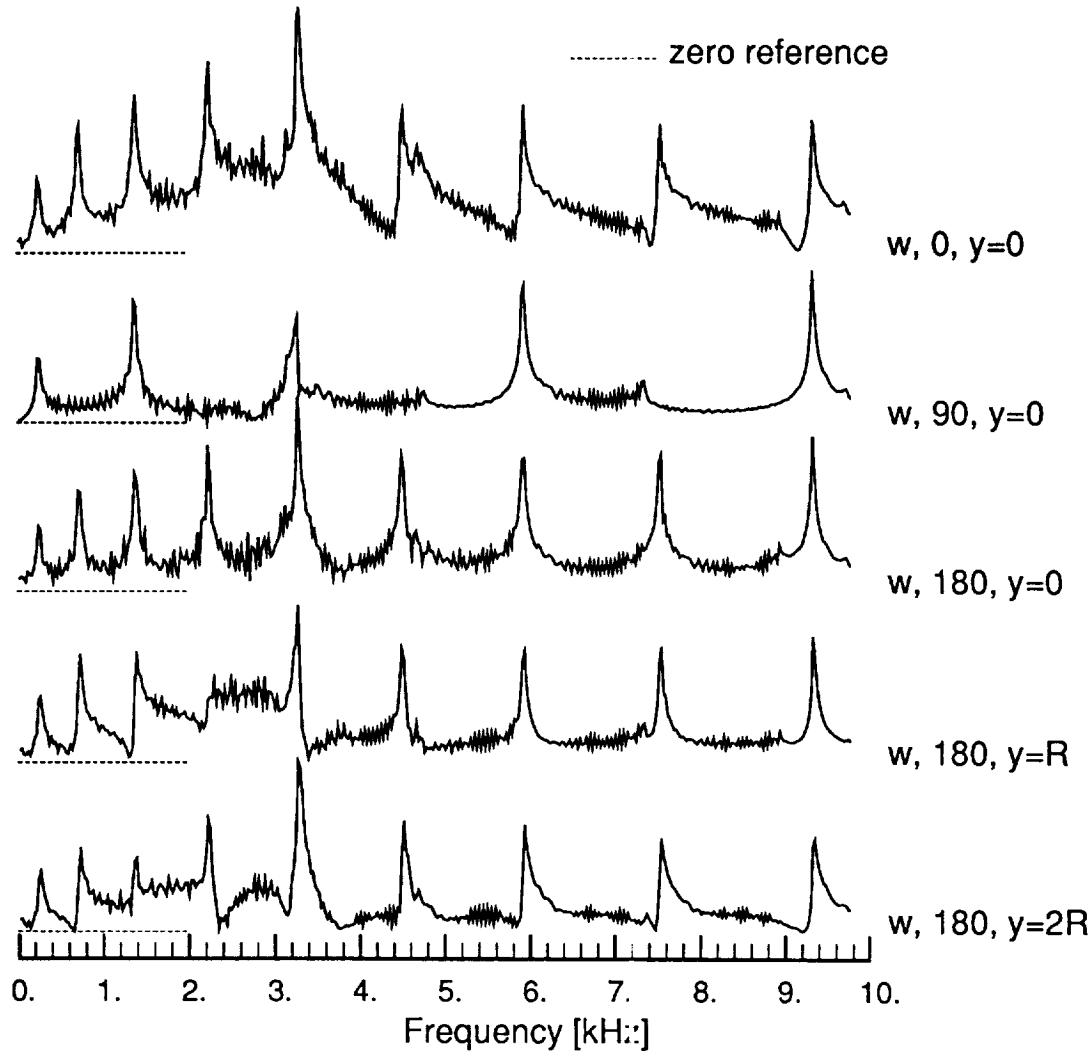

Figure 2.6: System response functions for the point excitation of a closed cylinder.

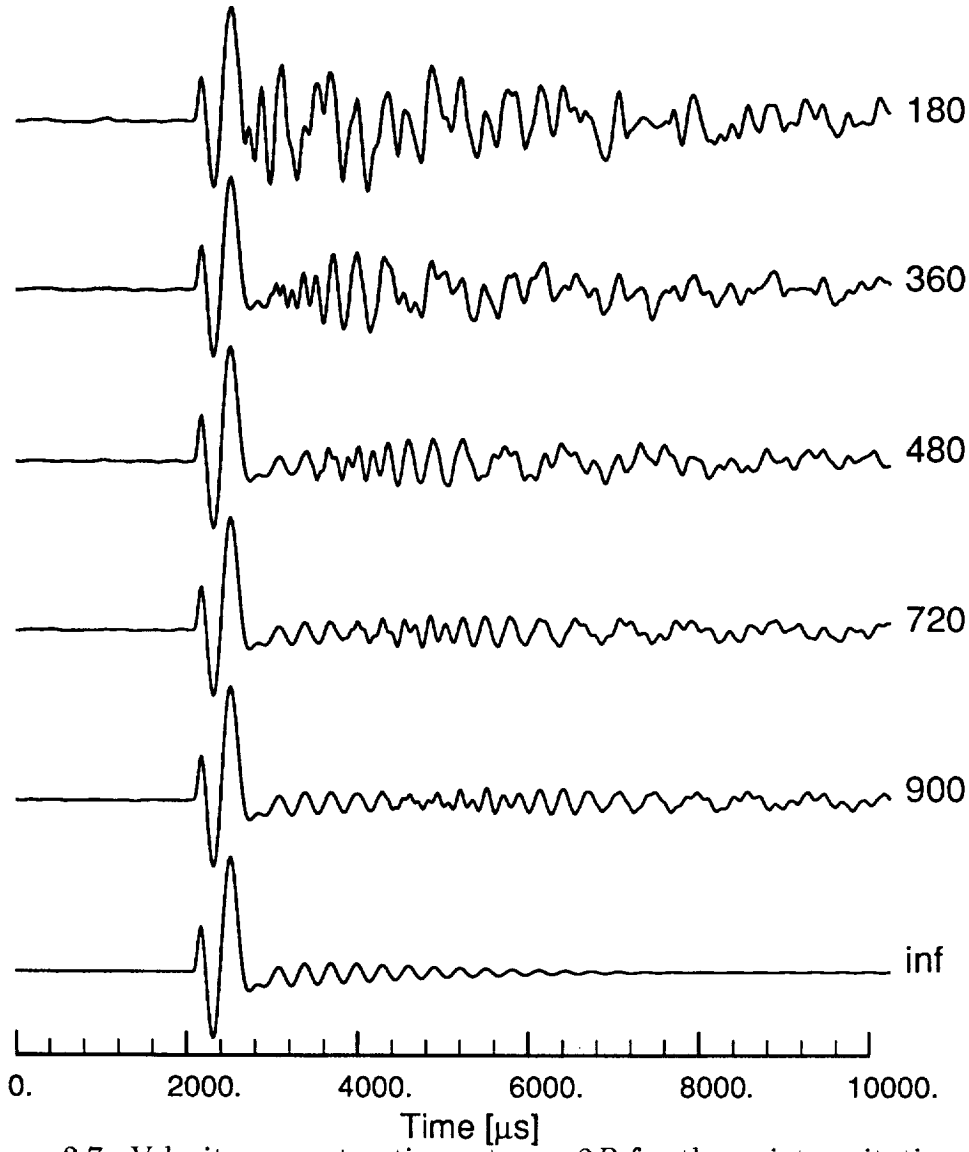

Figure 2.7: Velocity reconstructions at $y = 2R$ for the point excitation of shells of different circumference.

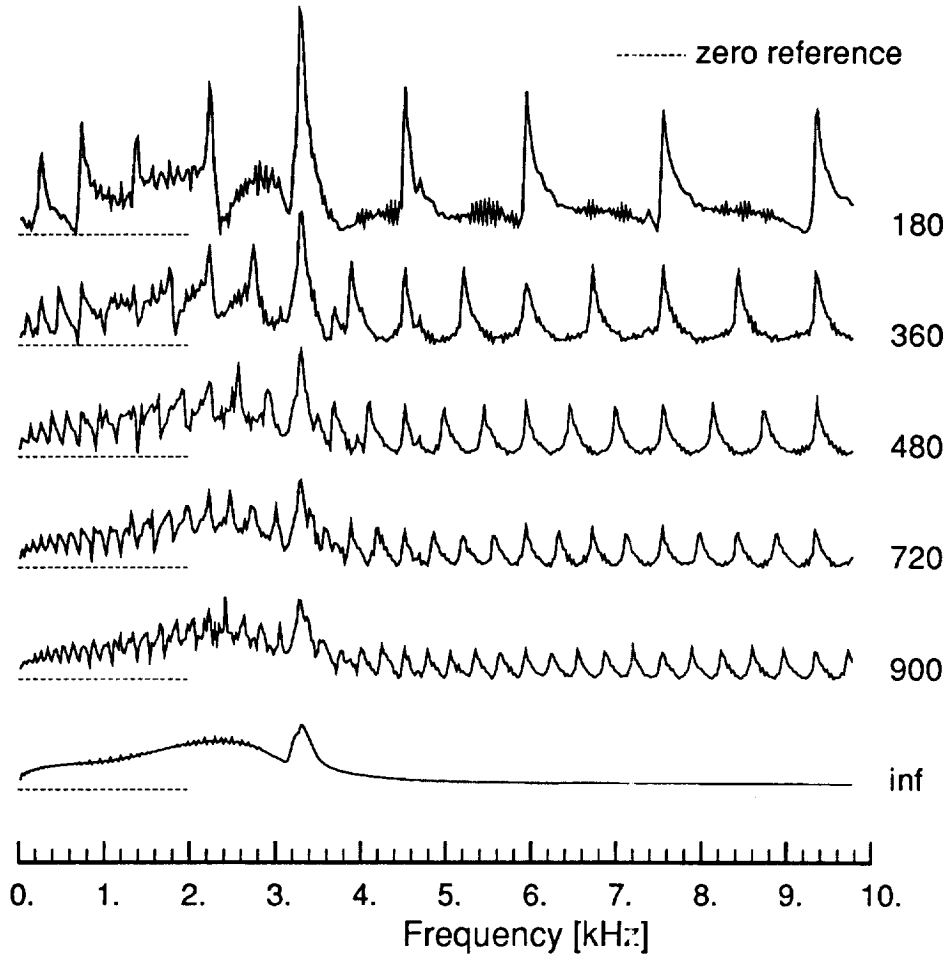

Figure 2.8: Frequency domain response at $y = 2R$ for the point excitation of shells of different circumference.

Chapter 3

Acoustic Radiation from Plate Structures

Spectral elements, which incorporate the effect of fluid loading on the structure, are developed for analyzing acoustic radiation from dynamically loaded extended plates. These elements may be conveniently joined to form complex thin-walled structures composed of many segments.

3.1 Introduction

There are many practical situations where the interaction between the dynamics of a structure and a surrounding fluid is of great importance. The most obvious is noise; noise is the propagation of acoustic energy through the fluid. The interaction can also influence the response of the structure itself; examples include dams, chimney stacks, ships, fuselages, propellers, and transmission cables. Fluid Loading problems are very hard to solve exactly, and for geometries and configurations of practical interest it is essential to be able to make useful simplifying approximations [31]. The purpose of this paper is to introduce a method being developed for analyzing folded plate structures immersed in a fluid.

A schematic of the cross-section of the folded plate structures of interest is shown in Figure 3.1a; the plates extend in the y-direction. Such a structure when immersed in a fluid can experience three types of loading. The first is the structure-borne excitation caused by the propagating structural waves. The second is a pressure loading arising from some source within the fluid; this acts as a distributed external loading on the structure. The third load is the 'self-loading' or fluid loading caused by the moving structure interacting with the fluid. This also acts as a distributed pressure loading but, since the magnitude depends on the motion of the structure, it has the effect of coupling the structure and fluid motions. Additionally, these enclosed structures are viewed as having two distinct regions; an interior region and an exterior region. The interior region has loadings due to both the fluid and the radiation from the vibration of other plates, whereas, the exterior region only experiences loadings from the fluid. In this paper, we restrict the fluid to be only on the exterior of the structure so that we can concentrate on the structural dynamics, fluid loading, and radiation into the fluid. The reverberation problem for enclosed spaces is the subject of a later paper.

Our analysis of the structural dynamics is based on the spectral element method (References [6, 8, 11] give summaries of the approach as applied to frame structures) but applied to structures of extended areas. This application to thin-walled structures begins by combining the spectral analysis for in-plane wave responses [19] and out-of-plane flexural behavior [27] to form a matrix method approach for folded plate structures [22]. The variety of structural shapes encompassed was recently enhanced by adding a segmented curved shell element [32]. The method has some very useful characteristics. First, it is a frequency domain formulation. Second, it is geared toward handling very large areas. That is, it is a counterpoint to conventional ele-

ments which always model a region as a collection of very small sub-domains. Third, it is stiffness formulated. This means the process of assemblage to form complex structures is relatively easy.

The solid/fluid interaction problem is very intricate [33, 34, 35]; many of the finer points are covered in the excellent summary paper by Crighton [36]. The essential difficulty is that the two media are coupled in a convolution sense — this is unlike a plate on an elastic foundation, say. We tackle the interaction problem by incorporating the effect of fluid loading on the structure directly into the element formulation. In this way, the structural formulation for in vacuum dynamic response is unaffected. Our approach is approximate but is shown to be reasonably accurate for medium fluid loading. Radiation from these extended plates is handled very conveniently by utilizing the shape functions associated with the spectral elements. In fact, this computation of the pressure response in the fluid is performed as a post-processing operation. The challenge we have here is to match the motion of the finite plate to that of the fluid. But the domain for the fluid is (at least) the half space above the plate and is considerably larger than the length of the plate itself. Therefore, to match the plate and fluid boundaries, we must extend the plate boundary. We do this by assuming the displacements can be matched by imposing $w = 0$ outside of the finite plate. We further assume that this can always be done even if the plate is not physically baffled but is attached to other plate segments. The idea is illustrated in Figure 3.1b.

Our interest in this paper is on aspects of the structure/fluid interaction, therefore for simplicity, we take the plates and loading as being uniform in the y-direction. We also have in mind aeronautical structures as typified by aluminum in air — this corresponds to a relatively light fluid loading situation as compared to naval applications.

3.2 Plate/Fluid Interaction: Infinite Plate

As a prelude to considering finite plates, we first look at the response of an infinite plate with fluid loading on one side. This will allow us to establish the context of the approximations to be made in the next section. The plate lies in the $x-y$ plane, but for simplicity we take the plates and loading as being uniform in the y-direction.

The governing equations for the deflection $w(x,t)$ of a thin plate and the resulting pressure $p(x,t)$, when a mechanical loading $q(x,t)$ is applied, are

$$D\frac{\partial^4 w}{\partial x^4} + \eta h\frac{\partial w}{\partial t} + \rho h\frac{\partial^2 w}{\partial t^2} = q(x,t) - p(x,z=0,t)\,, \qquad B\nabla^2 p = \rho_a\frac{\partial^2 p}{\partial t^2} \tag{3.1}$$

where h is the plate thickness, D the plate stiffness, ρ the plate mass density, B the fluid bulk modulus, and ρ_a the fluid mass density. We have also added some damping to the structure through η. The interface conditions between the plate and fluid are

$$w_{plate}(x) = w_{fluid}(x,z=0)\,, \qquad \frac{\partial p(x,z=0)}{\partial z} = -\rho_a\frac{\partial^2 w(x,z=0)}{\partial t^2} \tag{3.2}$$

Our solution technique uses spectral analysis; this assumes solutions of the form

$$w(x,t) = \sum_n^N \hat{w}(x,\omega_n)e^{i\omega_n t}\,, \qquad p(x,z,t) = \sum_n^N \hat{p}(x,z,\omega_n)e^{i\omega_n t}\,, \qquad \omega_n \equiv \frac{n2\pi}{T} \tag{3.3}$$

where T is the time window for the discrete transform. Typically, N ranges as $512 \approx 4096$. When these are substituted into the governing differential equations, we get

$$D\frac{d^4\hat{w}(x)}{dx^4} - \rho h\bar{\omega}^2\hat{w}(x) = \hat{q}(x) - \hat{p}(x,z=0)\,, \qquad B\nabla^2\hat{p} + \rho_a\omega^2\hat{p} = 0 \tag{3.4}$$

where $\bar{\omega}^2 = \omega^2 - i\omega\eta/\rho$ and the interface relations become

$$\hat{w}_{plate}(x) = \hat{w}_{fluid}(x,z=0)\,, \qquad \frac{\partial\hat{p}(x,z=0)}{\partial z} = \omega^2\rho_a\hat{w}(x) \tag{3.5}$$

This set of equations will be our primary equations governing the dynamic response of the plate and fluid.

Consider a single infinite sheet with fluid only on one side and with a line loading along $x=0$. Let the plate deflection and loading be represented in the form

$$\hat{w}(x) = \sum_m^M \tilde{w}_m e^{-i\xi_m x}\,, \qquad \hat{q}(x) = \sum_m^M \tilde{q}_m e^{-i\xi_m x}\,, \qquad \xi_m \equiv \frac{m2\pi}{W} \tag{3.6}$$

where W is the space window for the discrete transform. Typically, M ranges as $500 \approx 2000$. The pressure has a similar representation, except that we must realize it is two-dimensional

$$\hat{p}(x,z) = \sum_m^M \tilde{p}_m e^{-i\xi_m x}e^{-ik_z z}\,, \qquad k_z \equiv \sqrt{k_a^2 - \xi_m^2} \tag{3.7}$$

This corresponds to pressure waves radiating from the plate surface in the positive z-direction. The pressure boundary condition at $z = 0$ is now

$$-ik_z\tilde{p}_m = \rho_a\omega^2\tilde{w}_m$$

Substituting these into Equation (3.4) gives the displacement of the plate and the pressure in the fluid as, respectively,

$$\begin{aligned}\hat{w}(x) &= \sum_m \frac{\tilde{q}_m e^{-i\xi_m x}}{[D\xi_m^4 - \rho h\omega^2 + i\omega\eta h - \frac{\rho_a\omega^2}{ik_z}]} \\ \hat{p}(x,z) &= \sum_m \frac{\tilde{q}_m e^{-i\xi_m x}}{[D\xi_m^4 - \rho h\omega^2 + i\omega\eta h - \frac{\rho_a\omega^2}{ik_z}]\frac{-ik_z}{\rho_a\omega^2}}\end{aligned} \tag{3.8}$$

As with the case of a plate in a vacuum, $\tilde{q}_m$ is chosen to be 1.0 to represent a line load at $x = 0$.

Figure 3.2a shows the resulting pressures $100\,mm$ from a $2.5\,mm$ thick aluminum plate subjected to a line loading. The history of the loading is a smoothed triangular pulse of duration about $150\,\mu s$ and having frequency content of about $16\,kHz$. The pressures exhibit an oscillatory behavior where the period of the zero crossings is almost constant. Figure 3.2b looks at the system response function $|\hat{G}|$ where the pressure is related to the applied resultant load as $\hat{p} = \hat{G}\hat{P}$. The most striking feature of the pressure is the spectral peak in the vicinity of $5\,kHz$ — this corresponds to the coincidence frequency as discussed next. Note that the peak gets sharper further away from the impact site, and that there is more filtering before the coincidence frequency.

The coincidence frequency occurs when the phase speeds of the plate bending wave and of the acoustic wave in the fluid are equal [33, 34] and is given by

$$\omega_c = c_a^2\sqrt{\frac{\rho h}{D}} = \frac{c_a^2}{c_o h}\sqrt{12(1-\nu^2)}\,, \qquad c_o \equiv \sqrt{\frac{E}{\rho}}\,, \qquad c_o \equiv \sqrt{\frac{B}{\rho_a}} \tag{3.9}$$

The significance of the coincidence frequency is that wave components in the plate above this frequency are radiated easily into the fluid as seen in Figure 3.2. The coincidence phenomena depends on the extent of fluid loading, thus it is useful to have a measure of this loading. Following Reference [36], fluid loading is characterized by two independent parameters: a mass ratio $\alpha = \rho_a c_a/\rho h\omega$ and a speed ratio $M = c/c_a = k_a/k$. We have $M = 1$ at coincidence. Both parameters are frequency dependent; we can arrange for only one parameter which is varied with ω by

introducing

$$\epsilon \equiv \frac{\rho_a c_a}{\rho h \omega_c} = \frac{\rho_a}{\rho}\frac{c_o}{c_a}/\sqrt{12(1-\nu^2)}$$

The parameter ϵ, called the intrinsic fluid loading parameter, is the same for all plates of a given material embedded in a given fluid. This is typically small with values such as

$$\text{steel/water: } 0.130\,, \qquad \text{aluminum/air: } 0.002$$

In the examples that follow, we are primarily interested in the aluminum/air case.

3.3 Waveguide Modeling with Fluid Loading

Our goal here is to formulate the structural dynamics problem in terms of a waveguide. If we can replace the wavenumber transform solution for the plate response given in Equation (3.8) with a waveguide solution then that saves a summation operation. But much more importantly, it allows us to terminate the waveguide and thereby we are in a position to assemble complex structures. The difficulty is that while the effect of the fluid loading is that of a distributed pressure, it's non-local character makes it different from the pressure caused by a distributed spring, say, and hence we must invoke special procedures.

To begin our construction of a plate waveguide, we ask if it is possible for free waves to propagate in the plate immersed in a fluid. That is, we seek wave solution for the plate of the form $\hat{w} = \tilde{w}e^{-ikx}$ when the loading q is zero. This implies a pressure response of

$$\hat{p} = \tilde{p}\, e^{-ikx}e^{-ik_z z}\,, \qquad k_z \equiv \sqrt{k_a^2 - k^2}\,, \quad k_a^2 \equiv \frac{\omega^2}{c_a^2}$$

It must be borne in mind that as long as k_z is chosen as above then irrespective of the value of k the fluid equations are satisfied. When both $\hat{w}$ and $\hat{p}$ are substituted into the governing equation we obtain the characteristic equation

$$(k^2 - \beta^2)(k^2 + \beta^2) - \frac{\rho_a \omega^2}{ik_z D} = 0\,, \qquad \beta^2 \equiv \sqrt{\frac{\varrho_r h}{D}} \tag{3.10}$$

The third term in the first equation describes the effect of the fluid loading. A detailed explanation of the significance of each term is given by Crighton [36] and the roots of this characteristic equation have been studied extensively in References [37, 38, 31]. Contour plots of the characteristic equation are shown in Figure 3.3. It is seen that there are four dominant roots similar to a plane in a plate.

When the response of Equation (3.8) is viewed as a contour integral [39] in the complex planes of Figure 3.3, it has contributions from the poles and a contribution which arises from the branch cut associated with k_z. This latter contribution is most significant at impact points and corners [36]. By neglecting this contribution, we would then in a position to replace the responses with just the pole contributions. That is, we will have a waveguide representation. To quantify this contribution, we consider the response of a $25\,mm$ thick steel plate in a fluid of density $138\,g/m^3$ and modulus $0.37\,GPa$ subjected to the pulse line loading. This gives an intrinsic fluid loading of $\epsilon = 0.020$ which is an order of magnitude larger than the cases of actual interest. Figure 3.4 shows the responses with and without the branch cut contribution.

The agreement of the two solutions is very good with some deviations occurring at the load site that are primarily in the low frequency range. This is confirmed at the large x locations. We therefore conclude that in the case of an aluminum plate in air the branch cut contribution can be neglected.

Numerical solutions for the roots of the characteristic equation are shown in Figure 3.5 as circles along with the in vacuum roots indicated as the dashed lines. These plots, which are for $2.5\,mm$ aluminum plates in air, show that the fluid loading primarily has the effect of altering the imaginary part of the first mode. We see that at coincidence and beyond, the effect is of increased viscous damping — this is consistent with the observation that the fluid is receiving more of the energy at these frequencies. But otherwise the behavior is very similar to the in vacuum behavior. That is, the pole contributions are associated with root k_1 which corresponds predominantly to the propagating flexural wave, and with root k_2 which corresponds predominantly to an evanescent flexural wave.

Making the assumption that there are only two dominant structural waves allows us to obtain approximate analytical expressions for the roots as

$$\begin{aligned} k_1 &\approx \pm\sqrt{\beta^2 + \frac{\rho_a\omega^2}{2Dik_{z1}\beta^2}}, \qquad k_{z1} \equiv \sqrt{k_a^2 - \beta^2} \\ k_2 &\approx \pm i\sqrt{\beta^2 + \frac{\rho_a\omega^2}{2Dik_{z2}\beta^2}}, \qquad k_{z2} \equiv \sqrt{k_a^2 + \beta^2} \end{aligned} \tag{3.11}$$

These approximations are also plotted in Figure 3.5. There is very good agreement with the exact numerical roots over the entire frequency range including the region near coincidence.

By incorporating the fluid loading term directly into the modified spectrum relations, we are now in a position to replace the double summation wavenumber transform solution by a single summation over frequency. This is useful when an enclosed structure is viewed as having two distinct regions; an interior region and an exterior region. The interior region has loadings due to both the fluid and the radiation from the vibration of other plates. However, the exterior region only experiences loadings from the fluid. Using the modified spectrum relations, the fluid loading for the exterior problem can be accounted for without considering the fluid response. In this way, the solid/fluid interaction problem is partially decoupled.

We conclude this section by illustrating the difference the waveguide formulation makes. The transverse displacement of one half of the infinite plate with two forward

propagating waves is expressed as

$$\hat{w}(x) = \mathbf{A}e^{-ik_1 x} + \mathbf{B}e^{-ik_2 x}$$

where k_1 and k_2 are the modified spectrum relations presented in Equation (3.11). The boundary conditions for this problem are that at $x = 0$ the slope of the plate is zero ($\partial\hat{w}/\partial x = 0$) and the applied load is related to the shear by

$$-\tfrac{1}{2}\hat{P} = \hat{V} = -D\frac{\partial^3 \hat{w}}{\partial x^3}$$

The response of the plate is then determined to be

$$\hat{w}(x) = \frac{\hat{P}}{2Dik_1(k_1^2 - k_2^2)}\left[e^{-ik_1 x} - \frac{k_1}{k_2}e^{-ik_2 x}\right] \tag{3.12}$$

where most quantities are frequency dependence. This solution is to be compared to Equation (3.8). The responses of Figure 3.4 were computed using this solution.

It is clear that the waveguide approximate modeling for plates in a surrounding fluid is accurate and efficient.

3.4 Modeling of Finite Plates in a Fluid

We now illustrate how the waveguide modeling allows us to tackle the very difficult problem of the response of finite plates in a fluid.

We begin by writing the general transverse displacement for a typical plate segment of length L in the form

$$\hat{w}(x) = \mathbf{A}e^{-ik_1x} + \mathbf{B}e^{-ik_2x} + \mathbf{C}e^{-ik_1(L-x)} + \mathbf{D}e^{-ik_2(L-x)}$$

where **A**, **B**, **C** and **D** are constants to be determined from the boundary conditions on the segment. Also, by using the modified spectrum relations, we claim that this adequately represents the behavior of a plate immersed in a fluid. It is advantageous, when dealing with finite or multiply connected structures, to use a solution formulation that already incorporates the connectivities. The end conditions on the plate segment are

$$\hat{w}(0) = \hat{w}_1\,, \qquad \frac{d\hat{w}(0)}{dx} = \hat{\psi}_1\,, \qquad \hat{w}(L) = \hat{w}_2\,, \qquad \frac{d\hat{w}(L)}{dx} = \hat{\psi}_2$$

Solving for the coefficients in terms of the nodal degrees of freedom allows the transverse displacement of the plate to be re-written in the form of a collection of shape functions

$$\hat{w}(x) = \hat{g}_1(x)\hat{w}_1 + \hat{g}_2(x)L\hat{\psi}_1 + \hat{g}_3(x)\hat{w}_2 + \hat{g}_4(x)L\hat{\psi}_2 \tag{3.13}$$

The frequency dependent shape functions $\hat{g}_j(x,\omega)$ are given as

$$\begin{aligned}
\hat{g}_1(x) &= [r_1\hat{h}_1(x) + r_2\hat{h}_2(x)]/\Delta \\
\hat{g}_2(x) &= [r_1\hat{h}_3(x) + r_2\hat{h}_4(x)]/\Delta \\
\hat{g}_3(x) &= [r_1\hat{h}_2(x) + r_2\hat{h}_1(x)]/\Delta \\
\hat{g}_4(x) &= -[r_1\hat{h}_4(x) + r_2\hat{h}_3(x)]/\Delta \\
r_1 &= i(k_1 - k_2)[1 - e^{-k_1L}e^{-k_2L}]\,, \quad r_2 = i(k_1 + k_2)[1 - e^{-k_1L}e^{-k_2L}]
\end{aligned} \tag{3.14}$$

where $\Delta = -(r_1^2 + r_2^2)$ and

$$\begin{aligned}
\hat{h}_1(x) &= +ik_2[e^{-ik_1x} - e^{-ik_2L}e^{-ik_1(L-x)}] - ik_1[e^{-ik_2x} - e^{-ik_1L}e^{-ik_2(L-x)}] \\
\hat{h}_2(x) &= -ik_2[e^{-ik_2L}e^{-ik_1x} - e^{-ik_1(L-x)}] + ik_1[e^{-ik_1L}e^{-ik_2x} - e^{-ik_2(L-x)}] \\
\hat{h}_3(x) &= [e^{-ik_1x} + e^{-ik_2L}e^{-ik_1(L-x)}] - [e^{-ik_2x} + e^{-ik_1L}e^{-ik_2(L-x)}] \\
\hat{h}_4(x) &= [e^{-ik_2L}e^{-ik_1x} + e^{-ik_1(L-x)}] - [e^{-ik_1L}e^{-ik_2x} + e^{-ik_2(L-x)}]
\end{aligned}$$

As an example, the shape functions $\hat{g}_1$ and $\hat{g}_2'$ are shown plotted in Figure 3.6 for a number of frequencies. The shape functions occur in pairs where $\hat{g}_3$ and $\hat{g}_4$ are the mirror images of $\hat{g}_1$ and $\hat{g}_2$, respectively. These shape functions are comparable

to those of the conventional finite element method except that they are frequency dependent and can represent very large areas. References [11, 32] illustrate how these are used as the basis for the spectral element representation of the folded plate structures, these references also show the assemblage procedures.

What we want to look at here is how a typical plate segment radiates pressure into the fluid. The challenge we have here is to match the motion of the finite plate to that of the fluid. But the domain for the fluid is (at least) the half space $z > 0$ and $-\infty < x < \infty$ which is considerably larger than the length of the plate. Therefore, to match the plate and fluid boundaries, we must extend the plate boundary in the x direction. If the finite plate is baffled, that is, extended on both sides with very stiff material, then the displacements can be matched by imposing $w = 0$ outside of the finite plate. We will assume that this can always be done even if the plate is not physically baffled but is attached to other plate segments. The schematic is shown in Figure 3.1b.

At the surface of the plate, $z = 0$, the fluid displacement must be equal to the plate displacement. By extending the plate deflection over the full space window of the fluid, we can then give it the spectral representation

$$\hat{w}(x) = \sum_m \tilde{w}_m e^{-i\xi_m x}$$

Applying this to the shape functions gives

$$\tilde{w}_m = \hat{w}_1 \tilde{g}_{1m} + L\hat{\psi}_1 \tilde{g}_{2m} + \hat{w}_2 \tilde{g}_{3m} + L\hat{\psi}_2 \tilde{g}_{4m}\,, \qquad \tilde{g}_{jm} = \int_W \hat{g}_j(x) e^{-i\xi_m x} dx \qquad (3.15)$$

These integrals are easily evaluated since $\hat{g}_j(x)$ contain only exponentials. The shape functions $\hat{g}_j(x)$ are zero outside the length of the plate element; this is equivalent to assuming each finite plate segment is baffled to infinity. The continuity of w_j and ψ_j between segments ensure continuity of the fluid field. The response of the fluid now has the spectral representation

$$\hat{w}(x,z) = \sum_m \tilde{w}_m e^{-ik_z z} e^{-i\xi_m x}\,, \qquad \hat{p}(x,z) = \sum_m \frac{\rho_a \omega^2}{-ik_z} \tilde{w}_m e^{-ik_z z} e^{-i\xi_m x}\,, \qquad k_z \equiv \sqrt{k_a^2 - \xi_m^2}$$

These, in combination with Equation (3.15), relate the fluid response at any point to the plate nodal degrees of freedom. If there are many plate segments, then the total response would be the sum of the contributions from each segment. We will illustrate these formulas with the example of a finite plate.

In piecing together the solution for the finite plate of Figure 3.1c, we treat the plate as having two segments with the boundary conditions

$$\text{segment 12:} \qquad w_1 = 0\, \psi_1 = 0;\; w_2 = w_o,\; \psi_2 = 0$$

$$\text{segment 23:} \qquad w_1 = w_o,\ \psi_1 = 0;\ w_2 = 0\,\psi_2 = 0$$

This leads to the solution for the fluid displacement written in terms of the central deflection of the plate as

$$\hat{w}(x,z) = \hat{w}_o \sum_m \left[\tilde{g}_{3m} e^{-i\xi_m(x+L)} + \tilde{g}_{1m} e^{-i\xi_m x}\right] e^{-ik_z z}$$

Note that the representation for the first plate segment must be shifted an amount L. The pressure is given by

$$\hat{p}(x,z) = \hat{w}_o \sum_m \frac{\rho_a \omega^2}{-ik_z} \left[\tilde{g}_{3m} e^{-i\xi_m(x+L)} + \tilde{g}_{1m} e^{-i\xi_m x}\right] e^{-ik_z z}$$

The shear relation at the load location is $\frac{1}{2}\hat{P} = -\hat{V} = D\hat{w}_o'''$. This gives the central deflection as

$$\hat{w}_o = \frac{\hat{P}}{2D\hat{g}_1'''(0)}$$

With reference to Figure 3.1c, it is worth emphasizing that although w is physically continuous at Node 2, the above representations have a discontinuity. That is, segment 12 is discontinuous to the right while Segment 23 is discontinuous to the left. Hence this example is a good first test case of our scheme.

To test the validity of our approximations, a planar finite element model of a baffled plate in a fluid was constructed for the problem shown in Figure 3.1c; only a finite fluid domain was modeled. The plate is $25\,mm$ thick steel and the fluid has the properties such that $\epsilon = 0.02$. Figure 3.7 shows a comparison of velocities of the plate and the fluid. The agreement is quite good up to the time when reflections come from the far boundaries of the fluid — the spectral solution has no such boundaries. The agreement is especially good for our purpose when it is realized that the fluid loading corresponds to a loading factor nearly ten times that of our cases of interest of aluminum plates in air.

These equations were also applied to the case of a finite $2.5\,mm$ thick aluminum plate in air. The responses for the plate are shown in Figure 3.8; the presence of multiple reflections are obvious. Figure 3.9 shows the corresponding frequency domain behavior where the reflections give rise to multiple spectral peaks. Also shown are the resonance frequencies for a vibrating plate in vacuum, it is clear that the impact has excited many of the symmetric modes of vibration. The pressure responses for the fluid can also be seen in Figure 3.8. Similar to the plate response, these indicate the presence of multiple reflections occurring in the plate. This figure also indicates that the baffled finite plate not only excites the fluid directly in front of it but also at

a distance along the baffle. The pressure at $x = 2L$, $z = 0$ is non-zero even though the plate is baffled at that location — this is further indication that, in fluids, the relation between the pressure and displacement is non-local. The frequency domain depiction of these responses is shown in Figure 3.9. It can be seen that the frequencies at which the structural resonances were present in Figure 3.9 are readily transmitted into the fluid.

Intuitively, we might have thought that the response should be largest along a line normal to the plate. The responses shown in Figure 3.8 indicate that this is not so. Furthermore, Figure 3.9 shows that it is even frequency dependent. Figure 3.10 shows the directivity patterns at a number of frequencies; the near field behavior was computed from the full solution with $r = 2L$. It is clear that these patterns are very sensitive to direction when the frequency gets close to coincidence. Also shown are the deflected shapes of the plate at each frequency. These shapes indicate an almost sinusoidal plate deflection except at the center and edges — these are the points of significant radiation.

3.5 Discussion

The methods discussed in this paper is a first step in extending the spectral element method to include structure/fluid interaction problems. The key step is that by incorporating the fluid loading into the spectrum relations allows us to maintain the element formulation. This is important because the spectral element approach presents itself as a well founded matrix method that embodies a number of efficiencies we have long associated with the conventional finite element method. For the range of problems they are suited for, the spectral elements have been shown to conveniently model wave propagation in structures made of multiple panels. Furthermore, the spectral element is eminently suited for hosting on massively parallel computers [28, 21].

There are many more developments needed. The most important of them are: Verify the radiation approximation from re-entrant edges, Implement radiation from curved surfaces, and, Implement the book-keeping necessary for solving reverberation in a enclosed space. We will to report on these developments in future papers.

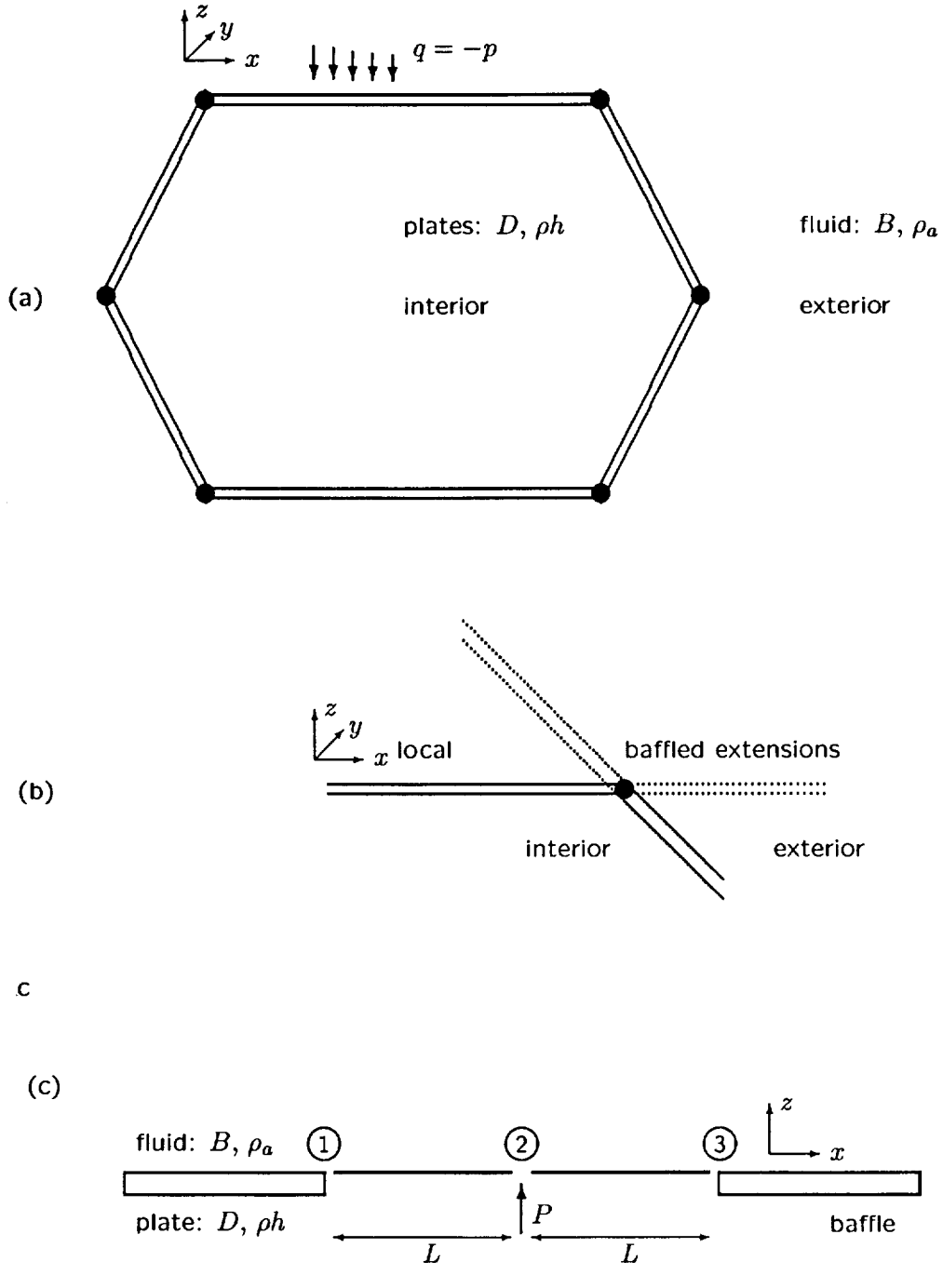

Figure 3.1: Geometries of the plate structures with fluid loading. (a) Schematic of cross-section of folded plate structures of interest. (b) Treatment of plate connections as baffled extensions. (c) Modeling of a finite baffled plate as two plate segments.

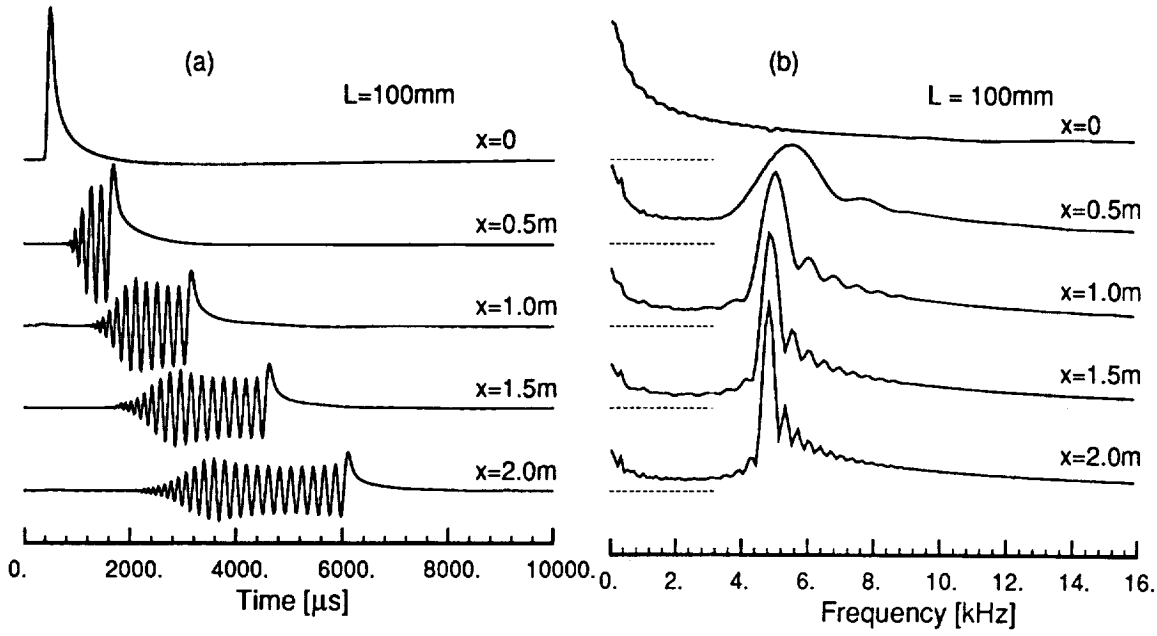

Figure 3.2: Time and frequency domain responses for the line loading of an infinite plate. (a) Fluid pressures $p(x, z = L, t)$. (b) System response function $|\hat{G}(x, z = L)|$ for pressure.

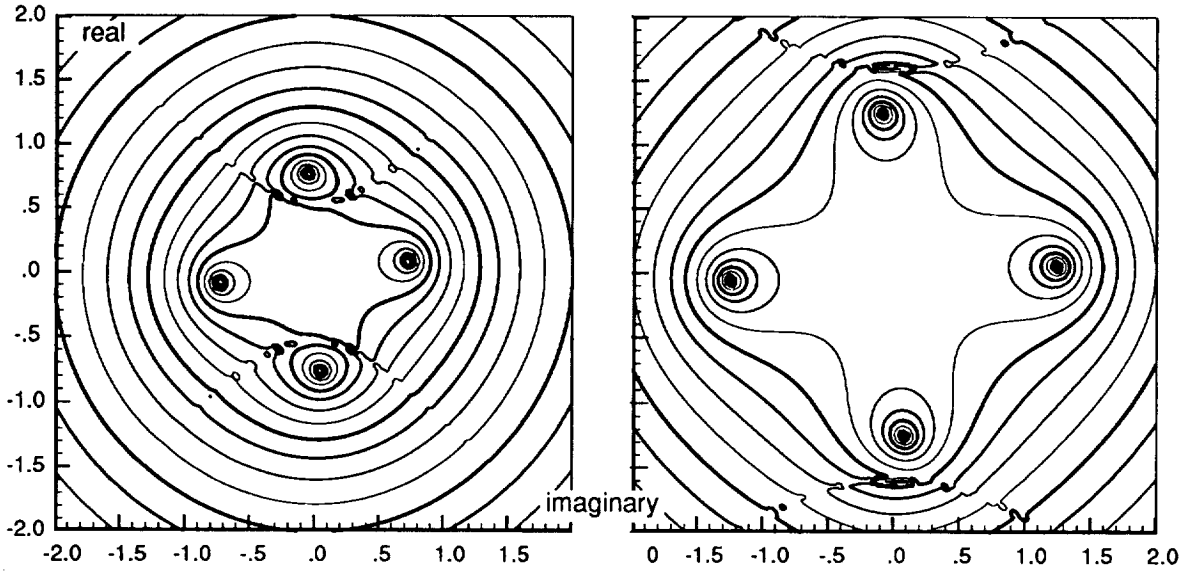

Figure 3.3: Contours of the characteristic equation for two frequencies straddling coincidence.

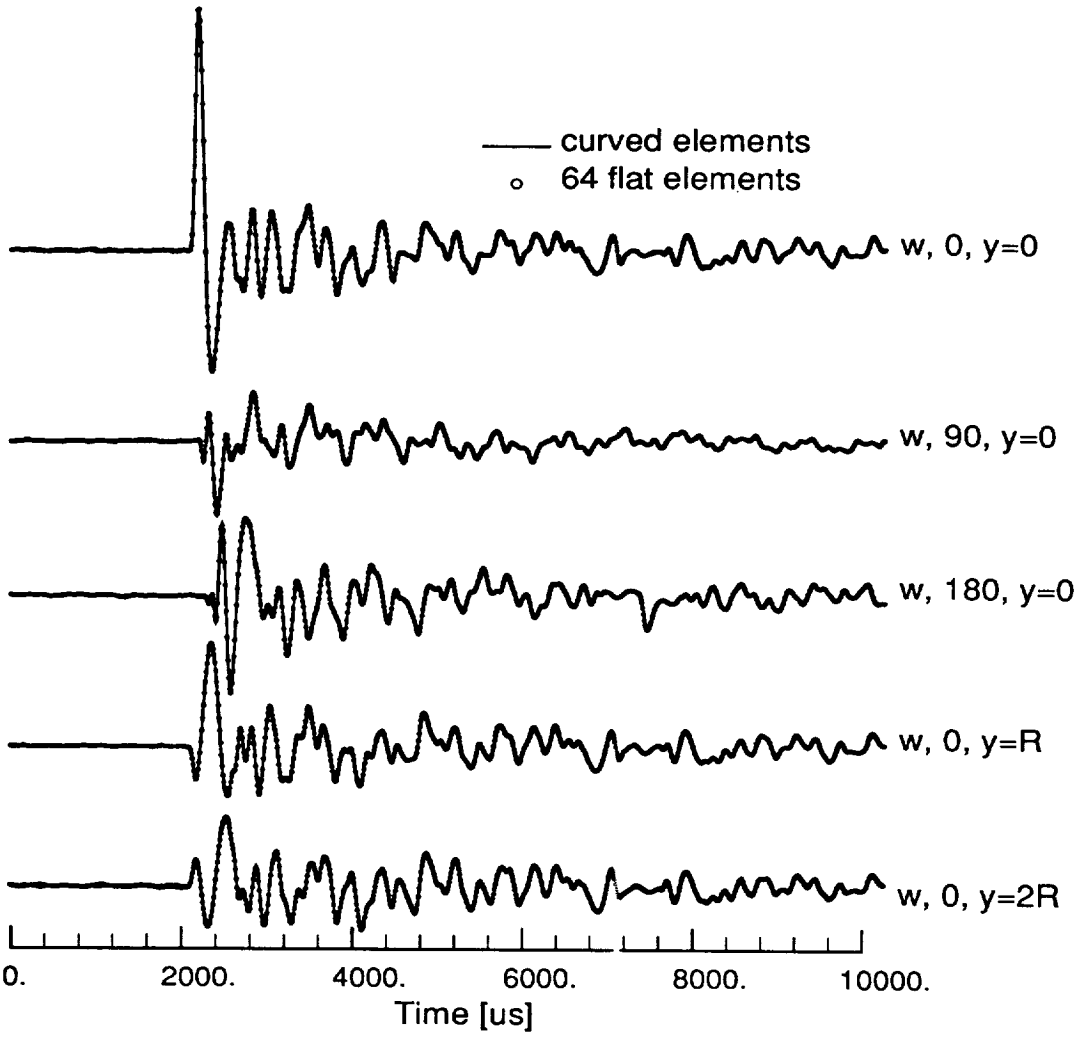

Figure 3.4: Comparison of the wavenumber transform solution to the waveguide solution that neglects the branch cut contribution.

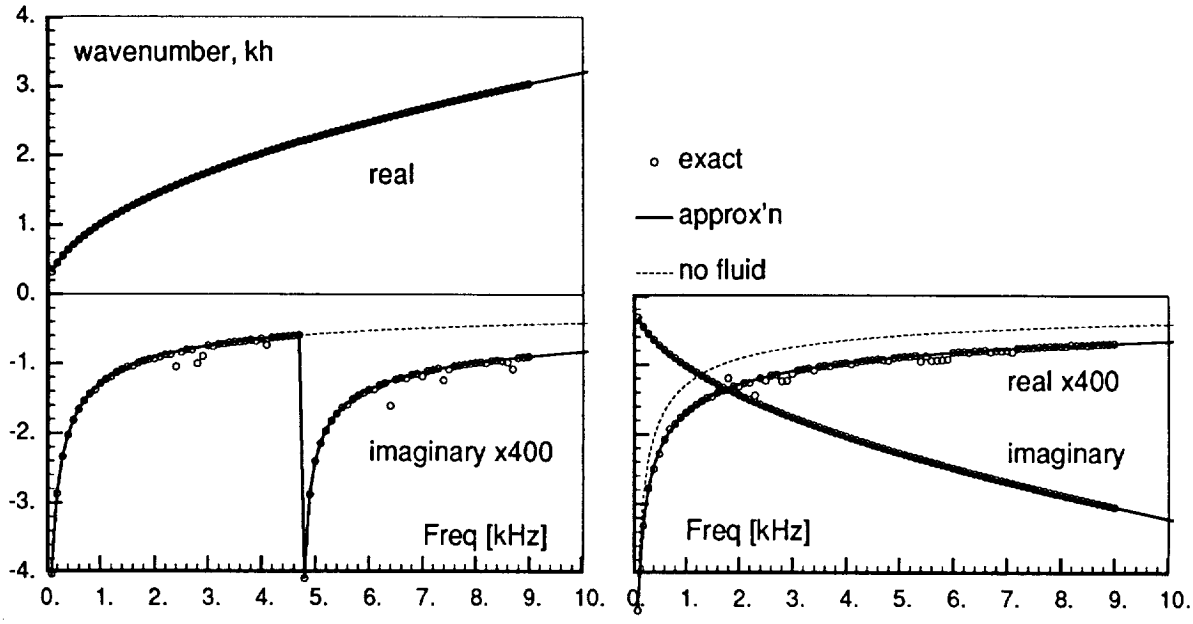

Figure 3.5: Wavenumber behavior for an aluminum plate in air. Left is $k_1(\omega)$, right is $k_2(\omega)$.

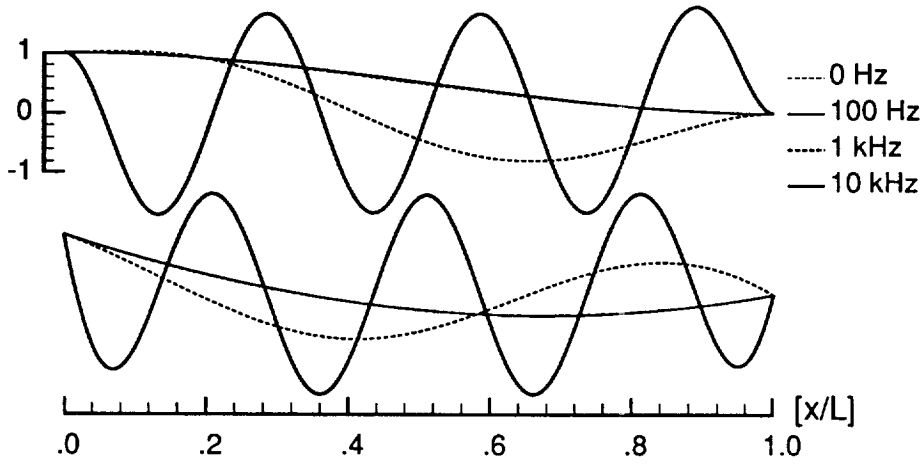

Figure 3.6: Shape functions $\hat{g}_1(x)$ (top) and $\hat{g}_2'(x)$ (bottom) for a number of frequencies.

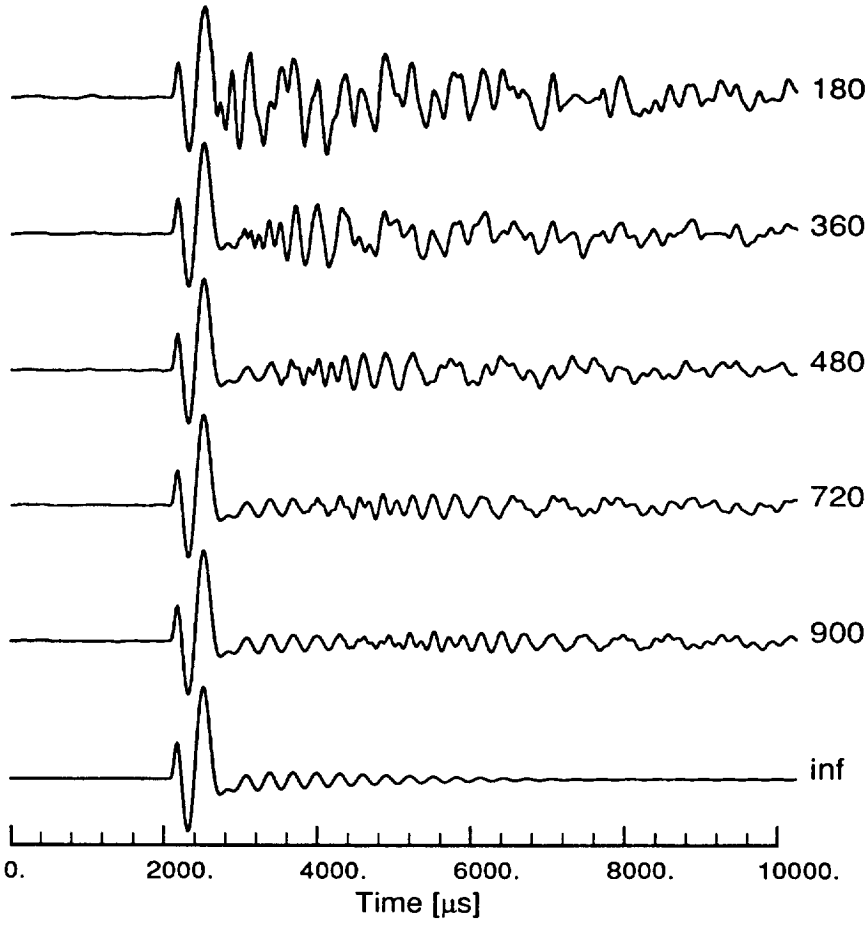

Figure 3.7: Response with modified spectrum relations and comparison with finite element solution.

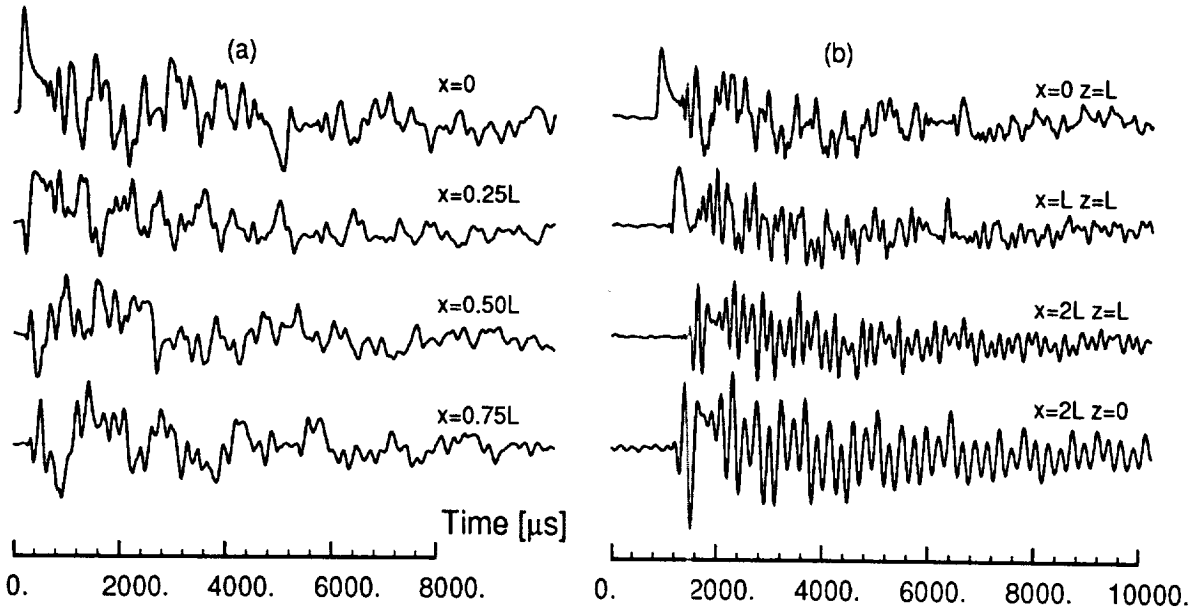

Figure 3.8: Time domain responses for a line loaded aluminum plate of length $2L = 500\,mm$. (a) Plate responses $\dot{w}(x,t)$, (b) fluid pressures $p(x, z = L, t)$.

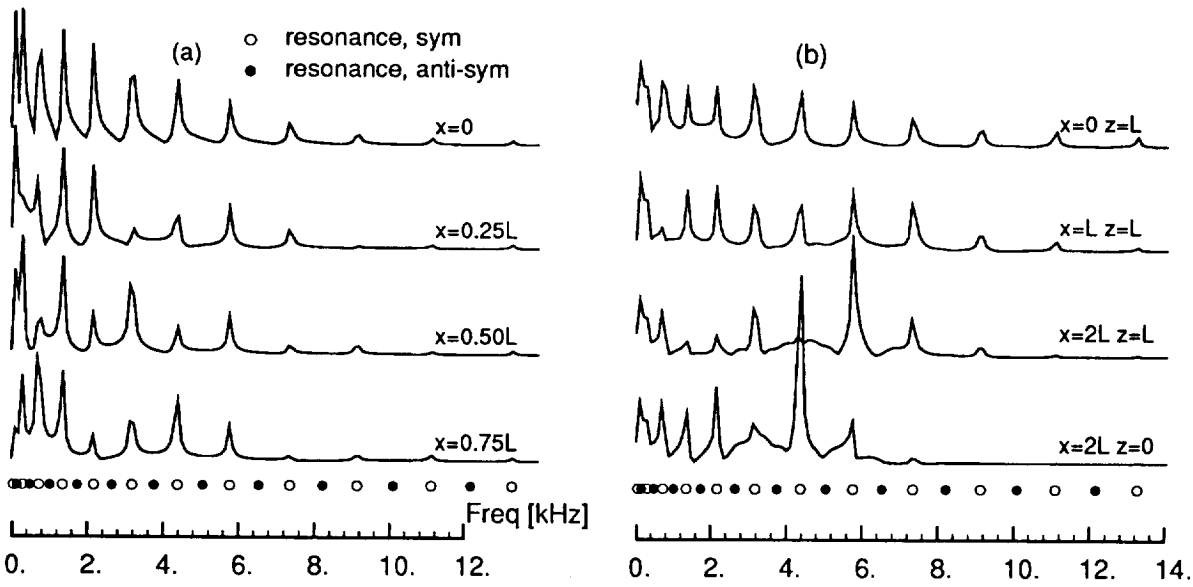

Figure 3.9: Frequency domain responses for an impacted plate of length $2L = 500\,mm$. (a) Plate responses $|i\omega\hat{w}(x)|$, (b) fluid pressure $|\hat{p}(x, z = L)|$.

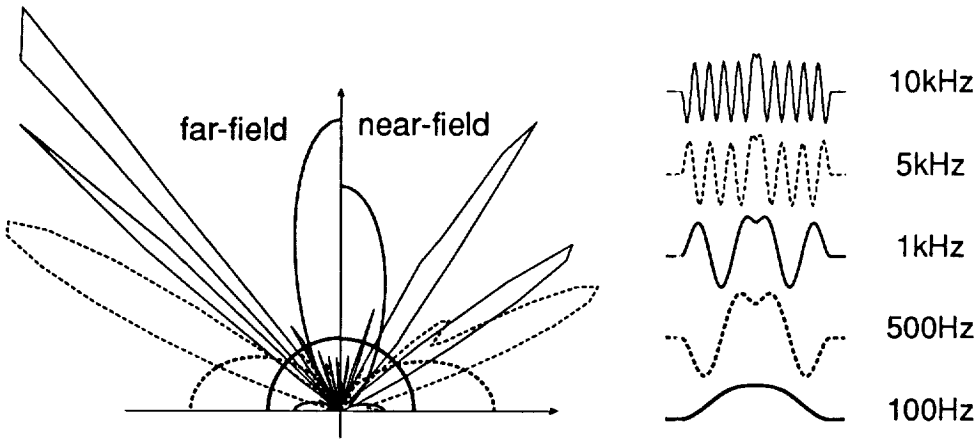

Figure 3.10: Directivity patterns for impacted finite plate. Also shown are the plate shapes at each frequency.

Bibliography

[1] **Philipson, L.L.**, On the Role of Extension in the Flexural Vibrations of Rings, *Journal of Applied Mechanics*, **23**, pp. 364–366, 1956.

[2] **Morely, S.D.**, Elastic Waves in a Naturally Curved Rod, *Quarterly Journal of Mechanical and Applied Mathematics*, **14**, pp. 155–172, 1961.

[3] **Wittrick, W.H.**, On Elastic Wave Propagation in Helical Springs, *International Journal of Mechanical Science*, **8**, pp. 25–47, 1966.

[4] **Britton, W.G.B. and Langley, G.O.**, Stress Pulse Dispersion in Curved Mechanical Waveguides, *Journal of Sound and Vibration*, **7**(3), pp. 417–430, 1968.

[5] **McConnell, K.G. and Chang, C.N.**, A Study of the Axial-Torsional Coupling Effect on a Sagged Transmission Line, *Experimental Mechanics*, **26**, pp. 324–329, 1986.

[6] **Gopalakrishnan, S., Martin, M.T. and Doyle, J.F.**, A Matrix Methodology for Spectral Analysis of Wave Propagation in Multiple Connected Timoshenko Beams, *Journal of Sound and Vibration*, pp. 11–24, 1992.

[7] **Gopalakrishnan, S. and Doyle, J.F.**, Wave Propagation in Connected Waveguides of Varying Cross Section, *Journal of Sound and Vibration*, **175**(3), pp. 347–363, 1994.

[8] **Martin, M.T., Gopalakrishnan, S. and Doyle, J.F.**, Wave Propagation in Multiply Connected Deep Waveguides, *Journal of Sound and Vibration*, **174**(4), pp. 521–538, 1994.

[9] **Gendy, A.S. and Saleeb, A.F.**, Vibrational Analysis of Coupled Extensional/Flexural/Torsional Modes of Curved Beams with Arbitrary Thin-walled Sections, *Journal of Sound and Vibration*, **174**(2), pp. 261–274, 1994.

[10] **Yang, S.Y. and Sin, H.C.**, Curvature-Based Beam Elements for the Analysis of Timoshenko and Shear-Deformable Curved Beams, *Journal of Sound and Vibration*, **187**(4), pp. 569–584, 1995.

[11] **Doyle, J.F.**, *Wave Propagation in Structures, 2/E*, Springer-Verlag, New York, 1997.

[12] **Doyle, J.F.**, *Static and Dynamic Analysis of Structures*, Kluwer, The Netherlands, 1991.

[13] **Doyle, J.F. and Farris, T.N.**, A Spectrally Formulated Finite Element for Wave Propagation in 3-D Frame Structures, *International Journal of Analytical and Experimental Modal Analysis*, **5**, pp. 223–237, 1990.

[14] **Abramowitz, M. and Stegun, I. A.**, *Handbook of Mathematical Functions*, Dover, New York, 1965.

[15] **Press, W.H., Flannery, B.P., Teukolsky, S.A. and Vetterling, W.T.**, *Numerical Recipes, 2nd ed.*, Cambridge University Press, Cambridge, 1992.

[16] **Gould, P.L.**, *Analysis of Plates and Shells*, Springer-Verlag, New York, 1988.

[17] **Leissa, A.W.**, *Vibration of Shells*, NASA SP-288, 1973.

[18] **Markus, S.**, *Mechanics of Vibrations of Cylindrical Shells*, Elsevier, New York, 1988.

[19] **Rizzi, S.A. and Doyle, J.F.**, Spectral Analysis of Wave Motion in Plane Solids with Boundaries, *Journal of Vibration and Acoustics*, **114**, pp. 133–140, 1992.

[20] **Rizzi, S.A. and Doyle, J.F.**, A Spectral Element Approach to Wave Motion in Layered Solids, *Journal of Vibration and Acoustics*, **114**, pp. 569–577, 1992.

[21] **Danial, A.N. and Doyle, J.F.**, Dynamic Response of Folded Plate Structures on a Massively Parallel Computer, *Journal of Computers and Structures*, **54**, pp. 521–529, 1995.

[22] **Danial, A.N., Rizzi, S.A. and Doyle, J.F.**, Dynamic Analysis of Folded Plate Structures, *Journal of Vibration and Acoustics*, **118**, pp. 591–598, 1996.

[23] **Hinton, E., Ozakca, M., and Rao, N.V.R.**, Free Vibration Analysis and Shape Optimization of Variable Thickness Plates, Prismatic Folded Plates and Curved Shells, Part 1: Finite Strip Formulation, *Journal of Sound and Vibration*, **181**(4), pp. 553–566, 1995.

[24] **Reissner, E.**, Stress and Displacement of Shallow Spherical Shells, *Journal of Mathematical Physics*, **25**(1), pp. 80–85, 1946.

[25] **Naghdi, P.M. and Berry, J.G.**, On the Equations of Motion of Cylindrical Shells, *Journal of Applied Mechanics*, **21**(2), pp. 160–166, 1964.

[26] **Bilodeau, B.A. and Doyle, J.F.**, A Spectral Element for Wave Propagation in Deep Curved Beams and Rings, *Journal of Sound and Vibration, submitted*, 1997.

[27] **Danial, A.N. and Doyle, J.F.**, Transverse Impact of Damped Plates Near a Straight Edge, *Journal of Vibration and Acoustics*, **117**, pp. 103–108, 1995.

[28] **Danial, A.N. and Doyle, J.F.**, A Massively Parallel Implementation of the Spectral Element Method for Impact Problems in Plate Structures, *Computing Systems in Engineering*, **5**, pp. 375–388, 1994.

[29] **Langley, R.S.**, Wave Motion and Energy Flow in Cylindrical Shells", *Journal of Sound and Vibration*, **169**(1), pp. 29–42, 1994.

[30] **Bilodeau, B.A.**, *Application of Spectral Element Method to Interior Noise Problems*, M.S. Thesis, Purdue University, 1995.

[31] **Crighton, D.G., Dowling, A.P., Ffowcs Williams, J.E., Heckl, M. and Leppington, F.G.**, *Modern Methods in Analytical Acoustics: Lecture Notes*, Springer-Verlag, Berlin, 1992.

[32] **Bilodeau, B.A. and Doyle, J.F.**, Dynamic Response of Segmented Cylindrical Shell Structures, *Journal of Vibration and Acoustics, submitted*, 1997.

[33] **Fahy, F.J.**, *Sound and Structural Vibration: Radiation, Transmission and Response*, Academic Press, New York, 1985.

[34] **Junger, M.C. and Feit, D.**, *Sound, Structures, and their Interaction*, MIT Press, Cambridge, 1986.

[35] **Norton, M.P.**, *Fundamentals of Noise and Vibration Analysis for Engineers*, Cambridge University Press, Cambridge, 1989.

[36] **Crighton, D.G.**, The 1988 Rayleigh Medal Lecture: Fluid Loading — The Interaction between Sound and Vibration, *Journal of Sound and Vibration*, **133**(1), pp. 1–27, 1989.

[37] **Crighton, D.G.**, The Free and Forced Waves on a Fluid-loaded Elastic Plate, *Journal of Sound and Vibration*, **63**(2), pp. 225–235, 1979.

[38] **Crighton, D.G. and Innes, D.**, Low Frequency Acoustic Radiation and Vibration Response of Locally Excited Fluid-Loaded Structures, *Journal of Sound and Vibration*, **91**(2), pp. 293–314, 1983.

[39] **Nayak, P.R.**, Line Admittance of Infinite Isotropic Fluid-Loaded Plates, *Journal of Acoustical Society of America*, **47**(1), pp. 191–201, 1970.